Article

Pd Nanoparticle-Decorated Novel Ternary Bi$_2$O$_2$CO$_3$-Bi$_2$MoO$_6$-CuO Heterojunction for Enhanced Photo-electrocatalytic Ethanol Oxidation

Kamal Kanti Bera, Anupam Chowdhury, Shyamal Kanti Bera, Mahima Ranjan Das, Atanu Roy, Sachindranath Das, and Swapan Kumar Bhattacharya*
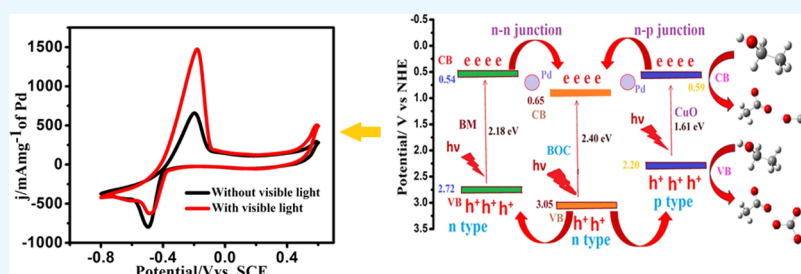
Read Online

ACCESS | 📊 Metrics & More | 📖 Article Recommendations | 🆂🅸 Supporting Information

ABSTRACT: Recently, photo-electrooxidation of fuel using a noble metal—semiconductor junction has been one of the most promising approaches in fuel cell systems. Herein, we report the development of a Pd-supported Bi$_2$MoO$_6$-Bi$_2$O$_2$CO$_3$-CuO novel ternary heterojunction for ethanol oxidation in alkali in the presence and absence of visible light. Various spectroscopic and microscopic characterization techniques confirm strong coupling between palladium nanoparticles and Bi$_2$MoO$_6$-Bi$_2$O$_2$CO$_3$-CuO ternary heterojunction supports. The photo-electrocatalytic efficacy of the synthesized catalysts was inspected by cyclic voltammetry (CV), chronoamperometry (CA), and electrochemical impedance spectroscopy (EIS). The CV study reveals that the forward peak current density (in mA mg^{-1} of Pd) of the synthesized quaternary heterojunction was about 1482.5, which is 2.4, 4, and 4.6 times higher than that of Pd/CuO (608.3), Pd/Bi$_2$MoO$_6$-Bi$_2$O$_2$CO$_3$ (368.3), and similarly synthesized Pd catalyst (321.5) under visible light radiation. The best heterojunction catalyst shows 2.21-fold higher peak current density in visible light compared to that in dark. CA study reveals that after operation for 6000 s, the current density of the quaternary electrode is 1.5 and 3.4 times greater than that of Pd/CuO and Pd/C catalysts, respectively. The greater photocurrent response, lower photoluminescence (PL) emission intensity, and smaller semicircle arc in the Nyquist plot of the quaternary catalyst demonstrate the efficient segregation and higher charge transfer conductance of photogenerated charges to facilitate the photo-electrooxidation process of ethanol. The stability test shows that the quaternary catalyst loses only 9.8 and 7.7% of its maximum current density after 500 cycles of CV operation in the dark and light, respectively, indicating that light energy is more beneficial in establishing high stability. The dramatic enhancement of the photo-electrocatalytic activity of the quaternary electrode is owing to the lower band gap, high ECSA, enhanced charge separation of photogenerated carriers (e$^-$—h$^+$), and all cocatalytic support of Bi$_2$MoO$_6$, Bi$_2$O$_2$CO$_3$, and CuO in Pd/ Bi$_2$MoO$_6$-Bi$_2$O$_2$CO$_3$-CuO under visible light radiation. The morphology and structure of the used quaternary catalyst are tested using FESEM and PXRD. Finally, ex situ FTIR spectroscopy and HPLC techniques help understand the ethanol electrooxidation reaction mechanism.

1. INTRODUCTION

Today, the fuel cell has been considered an alternative renewable clean energy source that mitigates simultaneously energy and environmental crises.[1] Among direct alcohol fuel cells (DAFCs), direct ethanol fuel cells (DEFCs) have been widely studied due to greater energy density, nontoxicity, low-temperature operation, easier transportation, large-scale production of fuel from agriculture products and biomass,[2−4] etc. Although the Pt-based electrocatalyst promotes the oxidation of alcohol, especially methanol and ethanol,[5−9] its potential commercialization is restricted due to its high cost, low abundance, and greater poisoning effect by carbonaceous

intermediates. However, the Pd-based anode is considered a substitute to Pt due to its less poisoning, cost effectiveness, greater durability in alkaline medium, and higher ability to combine with other metals or transition metal oxides. Earlier investigation shows that the ethanol oxidation reaction (EOR)
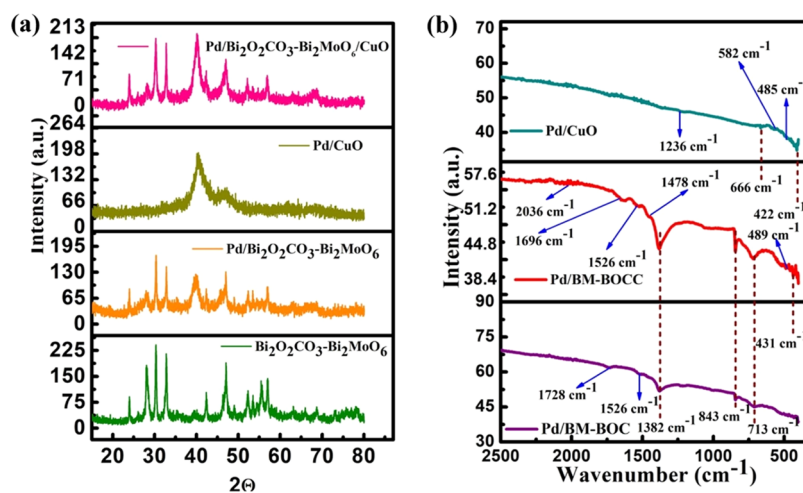
Figure 1. (a) PXRD patterns of Bi_2MoO_6-$Bi_2O_2CO_3$ (BM-BOC), Pd/Bi_2MoO_6-$Bi_2O_2CO_3$ (Pd/BM-BOC), Pd/CuO, and Pd/Bi_2MoO_6-$Bi_2O_2CO_3$-CuO (Pd/BM-BOCC) quaternary composites. (b) FTIR spectra of the synthesized Pd-modified catalysts.

can take place via a dual-pathway (C1 and C2) mechanism. The C1 pathway, total oxidation of ethanol, is utmost desired and difficult since it cleaves the C—C bond of ethanol and produces CO_3^{2-} in alkali by releasing 12 electrons. The C2 pathway is not effective as the EOR in this route is incomplete (delivering 2 or 4 electrons) and produces acetaldehyde and acetate in alkali.[9−12] Therefore, it is crucial to improve an advanced electrocatalyst that is able to disrupt the C—C bond. Recently, one of the most promising technologies to alter solar and chemical energy into electrical energy is photoassisted electrocatalysis of ethanol that utilizes noble metal/semiconductor junctions as the photo-electrocatalyst.[9−20] The nonnoble metal oxide is inexpensive, helps disperse metal nanoparticles easily, has good stability against dissolution, assists the bifunctional mechanism with oxygenated species, and facilitates the C—C bond cleavage for complete oxidation of ethanol to carbonate in alkali.[21] Indeed, semiconductor metal oxide has the capability of alcohol oxidation under light irradiation through synergistic electro- and photocatalytic processes.

In this concern, bismuth-based visible light-active semiconductors such as Bi_2MoO_6, $BiVO_4$, Bi_2WO_6, $BiPO_4$, $Bi_2O_2CO_3$, etc. appeared to be potential candidates because of having a strong response to visible light due to the narrow band gap energy and outstanding catalytic activity on photoexcitation.[22,23] $Bi_2O_2CO_3$ is an n-type newly developed semiconductor, nontoxic green photocatalyst consisting of a Aurivillius-type structure of alternate $Bi_2O_2^{2+}$ and CO_3^{2-} layers with a band gap of 3.3 eV.[24] On the other hand, Bi_2MoO_6 is an important Bi-based semiconductor that also belongs to the aurivillius-related oxide family comprising $Bi_2O_2^{2+}$ layers in octahedral sandwiched MoO_4^{2-} slabs, low cost, highly photostable, n-type semiconductor, and suitable band gap of 2.5−2.8 eV.[25] It has been used in a variety of applications such as photocatalysts, water splitting, CO_2 reduction, photo-electrocatalyst, gas sensing, supercapacitor, and energy storage device.[26−29] However, the application of pure $Bi_2O_2CO_3$ or Bi_2MoO_6 is still hindered because of its greater recombination rate of photogenerated e^-—h^+ pairs. To subdue these shortcomings, coupling of Bi_2MoO_6 with $Bi_2O_2CO_3$ semiconductors is a rational design. Various $Bi_2O_2CO_3$- and Bi_2MoO_6-based semiconductor heterojunctions such as $Bi_2O_3/Bi_2O_2CO_3$,[30] Pd/$Bi_2O_2CO_3$,[31] $Cu_2O/Bi_2O_2CO_3$,[32]

$Bi_2S_3/Bi_2O_3/Bi_2O_2CO_3$,[33] $Bi_2MoO_6/Bi_2O_2CO_3$,[34] Cu_2O-Bi_2MoO_6,[35] $Cu_2O/Bi/Bi_2MoO_6$,[36] $Ag-Bi_2O_2CO_3/Bi_{3.64}Mo_{0.36}O_{6.55}/Bi_2MoO_6$,[37] TiO_2 $Bi_2MoO_6\backslash Bi_{3.64}Mo_{0.36}O_{6.55}$,[38] etc. have been developed for improved photocatalytic activity. Xiang et al. synthesized 3D-heterostructured Ti-based $Bi_2MoO_6/Pd/TiO_2$[39] photocatalysts for solar light-driven photo-electrocatalytic hydrogen generation. Again, it is well known that Cu-based catalysts bring high activity and long life to the principal catalyst due to its lower binding affinity to CO species.[17,40] CuO is an easily synthesized, eco-friendly, p-type semiconductor (band gap of 1.7 eV), which has good porosity, chemical stability, excellent photochemical properties, low cost, and high abundance. It exhibits exciting applications in the field of energy conversion, storage, and sensors.[41,42] The structural integral of the p-type CuO semiconductor with n-type Bi_2MoO_6 and $Bi_2O_2CO_3$ semiconductors will be a new promising strategy to develop highly efficient visible light-driven photocatalysts. Recently, Wang et al.[43] synthesized a CuO/Bi_2MoO_6 hybrid nanosheet for toluene oxidation under solar radiation. In the literature, several studies reported that the copper oxide-supported Pd catalyst exhibits excellent catalytic activity and stability in the EOR,[17,40,44−46] facilitates the breaking of the C—C bond, and promotes the adsorption of OH^- species on the catalyst surface, which helps remove CO_{ads} species during oxidation.[47−49] Thus, copper oxide-based electrocatalysts can be used as a most promising candidate for alkaline DEFCs.

Inspired by the admirable visible light activity of Bi_2MoO_6, $Bi_2O_2CO_3$, and CuO in binary and ternary heterojunctions and considering the benefit from the synergistic effect between Pd and CuO, we herein design and fabricate Pd/Bi_2MoO_6-$Bi_2O_2CO_3$, Pd/CuO, and novel Pd/$Bi_2O_2CO_3$-Bi_2MoO_6-CuO photoanodes for electrocatalytic ethanol oxidation under visible light illumination. We synthesized the Bi_2MoO_6-$Bi_2O_2CO_3$ catalyst without using additional carbon sources. The results of the present work revealed that the quaternary heterojunction catalyst has much higher photo-electrocatalytic efficacy and stability toward ethanol oxidation and improved tolerance of CO compared to ternary and binary junctions Pd/$Bi_2O_2CO_3$-Bi_2MoO_6 and Pd/CuO. The multiple cycling test of CV under visible light exhibits that CuO favors the formation of an active PdO_x (x = 1,2) layer on the Pd surface, which leads to enhanced activity and excellent stability in photo-
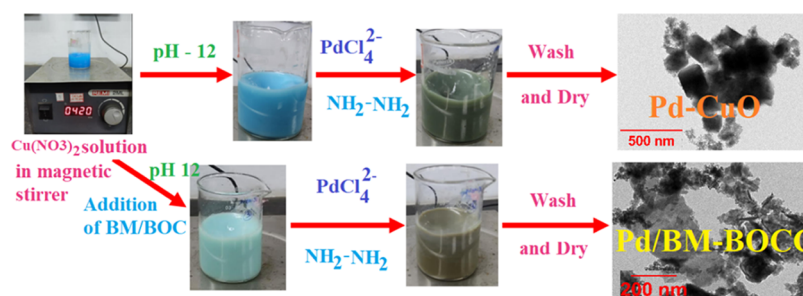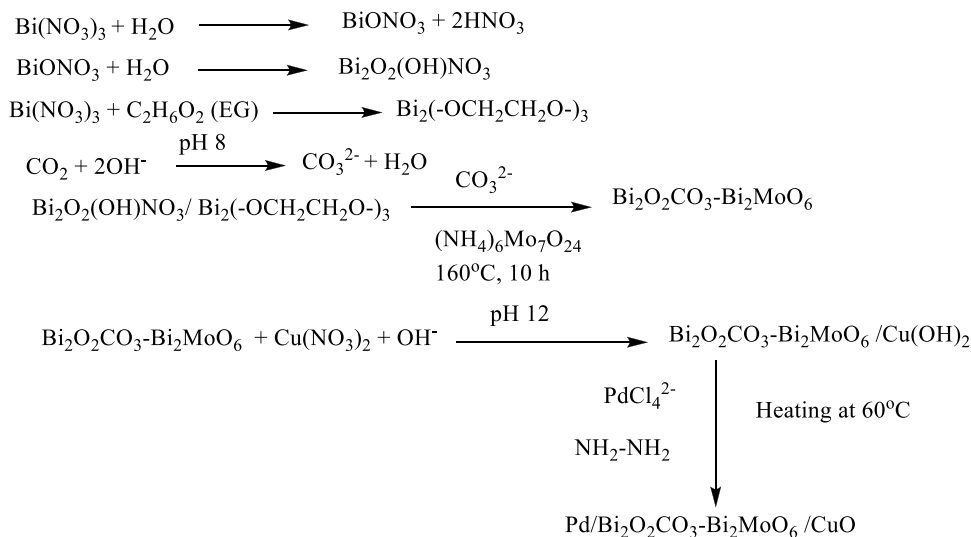
Figure 2. Representation of the synthetic procedure of Pd/CuO and Pd/BM-BOCC catalysts.

Scheme 1. Mechanism of Formation of the Pd/BM-BOCC Quaternary Catalyst

electrooxidation of ethanol in alkali. The identification of EOR products by ex situ FTIR and HPLC measurements indicates that the photo-electrooxidation process of ethanol undergoes both C1 and C2 pathways, leading to the formation of acetate and carbonate. This study offers a novel direction for the design of significantly stable and effective photo-electro-catalytic anode materials for electrocatalytic ethanol oxidation under visible light irradiation.

2. RESULTS AND DISCUSSION

2.1. Structural and Morphological Characterization.
The crystal structures of the as-synthesized Pd-modified CuO, $Bi_2O_2CO_3$-Bi_2MoO_6, and Bi_2MoO_6- $Bi_2O_2CO_3$/CuO hetero-junctions were recorded by PXRD and are shown in Figure 1a. The peaks corresponding to 2θ (/degree) at 19.4, 23.89, 30.26, 32.84, 35.24, 39.55, 42.29, 46.94, and 53.48 are ascribed to the (060), (121), (161), (002), (240), (0120), (280), (202), and (321) planes of orthorhombic $Bi_2O_2CO_3$ (JCPDS 84-1752), respectively. The peaks at 2θ values of 28.2, 32.65, 33.2, 46.54, 47.21, 55.3, 58.01, 68.60, 74.65, 76.05, and 78.01 are assigned to the (131), (200), (210), (202), (260), (331), (262), (341), (410), (144), (391), and (412) crystallographic planes of orthorhombic Bi_2MoO_6 (JCPDS 771246), respectively, and the peaks at 2θ of 40.23, 46.18, and 68.5 correspond to the planes of (111), (200), and (220) of the cubic Pd phase (JCPDS 894897). The diffraction peaks observed at 2θ 32.50, 35.41, 38.35, 46.26, 51.58, 53.48, 56.75, 58.46, 61.23, 67.35, 68.15, and 72.39 could be indexed to the (110), (002), (111), (-112), (112), (020), (021), (202), (-113), (113), (220), and

(311) planes of monoclinic CuO (JCPDS 895899), respectively. The distinguished peak of Pd, $Bi_2O_2CO_3$, Bi_2MoO_6, and CuO in Pd/$Bi_2O_2CO_3$·Bi_2MoO_6-CuO (Pd/BM-BOCC) reveals the formation of a quaternary hetero-junction synthesized by the solvothermal−chemical reduction method. The mass % of Pd, $Bi_2O_2CO_3$, Bi_2MoO_6, and CuO in the Pd/BM-BOCC catalyst is determined using Rietveld refinement[50,51] of PXRD data (Figure S1) and observed 22.6 wt % Pd, 33.61 wt % Bi_2MoO_6, 39.45 wt % $Bi_2O_2CO_3$, and 4.34 wt % CuO, which agree well with the experimental percentage.

FTIR spectral analysis of the as-synthesized heterostructures is depicted in Figure 1b. The bands located at 1728 and 1696 cm^{-1} are related to the stretching vibration of the −OH group in the surface-adsorbed water molecules.[52] The wavenumbers in the range of 400−1000 cm^{-1} may correspond to Bi−O, Mo−O, and Mo−O−O bridging−stretching vibration.[53−55] Particularly, the peaks observed at 843 and 713 cm^{-1} can be ascribed to the bending mode (out of plane) of the CO_3^{2-} group and symmetric stretching of MoO_6 involving the vibration of apical oxygen atoms, respectively.[54,56] The peaks around 1382 and 1478 cm^{-1} are recognized for the antisymmetric stretching mode of the CO_3^{2-} group.[34] The absorption bands located at 452 and 666 cm^{-1} are due to the Cu−O stretching vibration of CuO.[57] The presence of peaks at 844, 718, and 458 cm^{-1} in Pd/BM-BOCC supports the formation of the $Bi_2O_2CO_3$-Bi_2MoO_6-CuO heterostructure.

In the synthesis process, bismuth nitrate and ammonium molybdate solution were prepared in the mixed solvent

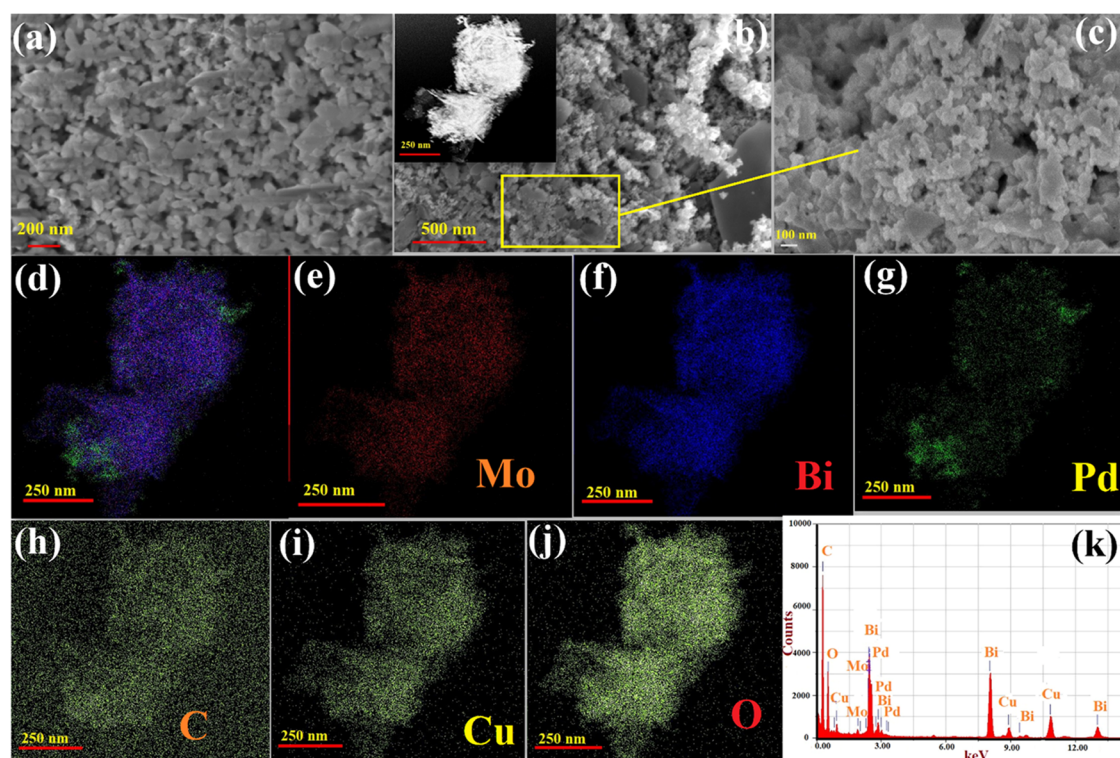**Figure 3.** FESEM images of Pd/Bi$_2$MoO$_6$-Bi$_2$O$_2$CO$_3$ (a) and Pd/Bi$_2$MoO$_6$-Bi$_2$O$_2$CO$_3$-CuO catalysts (b), inset of (b) and (c) elemental mapping images of the overlay of all elements (d), Mo (e), Bi (f), Pd (g), C (h), Cu (i), O (j), and EDX (k) from FESEM.

containing water:ethylene glycol (EG) (V/V) = 1:1. Bismuth nitrate pentahydrate on successive sonication and stirring processes hydrolyzes to Bi$_2$O$_2$(OH)NO$_3$ in water and makes Bi$_2$(−OCH$_2$CH$_2$O−)$_3$ complex in the EG solvent. When the solution taken in the autoclave followed by addition of (NH$_4$)$_6$Mo$_7$O$_{24}$ in basic conditions (pH 8) is heated at 160 °C for 10 h, EG easily decomposes into carbonate in the reaction system during the solvothermal process and Bi$_2$O$_2$(OH)NO$_3$ or Bi$_2$(−OCH$_2$CH$_2$O−)$_3$ gives rise to Bi$_2$O$_2$CO$_3$-Bi$_2$MoO$_6$ (BM/BOC) by in situ carbonization.[58,59] Chen et al. also synthesized Bi$_2$O$_2$CO$_3$ using the EG solvent in a solvothermal process without any additional carbon source. They proposed that EG easily decomposes into carbonate in the reaction system, which combined with bismuth oxide to form bismuth subcarbonate.[60] After the synthesis of the Bi$_2$O$_2$CO$_3$-Bi$_2$MoO$_6$ catalyst, this synthesized product is again mixed with copper nitrate in strong alkaline conditions; copper hydroxide is formed in the mixture, which on heating produces the Bi$_2$O$_2$CO$_3$-Bi$_2$MoO$_6$-CuO catalyst.[40] Again, the addition of PdCl$_4^{2-}$ followed by hydrazine hydrate produces the Pd/Bi$_2$O$_2$CO$_3$-Bi$_2$MoO$_6$-CuO heterojunction as shown in Figure 2 and Scheme 1. Here, the standard redox potential data of Pd^{2+}/Pd (0.915 V) and Cu^{2+}/Cu (0.34 V) reveal the reduction of Pd^{2+} and oxidation of Cu. The details of the Pd doping process on metal oxides or other metal are clearly explained in our previous studies and the literature.[2,4,10,16]

The morphologies of the as-prepared powder samples of Pd-Bi$_2$MoO$_6$-Bi$_2$O$_2$CO$_3$ (Pd/BM-BOC), and Pd-Bi$_2$MoO$_6$-Bi$_2$O$_2$CO$_3$-CuO (Pd/BM-BOCC) nanocatalysts were observed by FESEM (Figure 3a−c). In Figure 3a, a hierarchical morphology with a relatively smooth and flat surface and small spherical particles were found on the surface of Bi$_2$MoO$_6$-Bi$_2$O$_2$CO$_3$ in the Pd-BM-BOC catalyst, which may be due to the deposition of metallic Pd. The FESEM images of Pd-BM-

BOCC in different magnified scales are exhibited in Figures S2a and 3b,c. The rectangular yellow portion of Figure 3b is shown clearly in Figure 3c. All these figures indicate that the quaternary catalyst is the mixture of a typical morphology with a smooth and flat surface, flower-like agglomerates, and small spherical aggregated nanoparticles. The small spherical nanoparticles of metallic Pd were dispersed on the surface of the Bi$_2$MoO$_6$-Bi$_2$O$_2$CO$_3$-CuO heterojunction. The map scanning of the Pd-BM-BOCC nano-heterostructure (Figure 3d−j) exhibits that all the elements are almost uniformly distributed in the heterostructure. The EDX analysis of Pd/BM-BOC and Pd/BM-BOCC catalysts (Figures S3b and 3k) confirms the existence of Pd, Bi, C, Mo, and O elements in the ternary Pd/BM-BOC catalyst and Pd, Bi, C, Mo, Cu, and O elements in the Pd/BM-BOCC quaternary catalyst. The EDX elemental quantification analysis (Figures S2b and S3b) indicates 22.6 wt % Pd, which very closely matches with our experimental data.

The XPS study was accomplished to explore the chemical states of elements in the synthesized quaternary composite and is depicted in Figure 4. The survey spectra (Figure 4a) exhibit strong characteristic peaks of Pd, Bi, Cu, Mo, C, and O elements. The deconvolution spectrum of Pd (Figure 4b) shows two sets of spin−orbit doublets: the characteristic binding energies (BEs) of 335.2 and 340.6 eV can be assigned to 3d$_{5/2}$ and 3d$_{3/2}$ of metallic Pd (0) and other two peaks at 336.1 and 341.7 eV correspond to 3d$_{5/2}$ and 3d$_{3/2}$ of Pd^{2+}, respectively.[52,61] The atom percentage of Pd is calculated from the areas under the peak of Pd compared to the total area of other elements present in the quaternary catalyst and is found to be 22.8%.

The deconvoluted Bi spectrum comprised four peaks and is displayed in Figure 4c. The BEs at 157.2 and 162.5 eV are attributed to Bi^0 4f$_{7/2}$ and 4f$_{5/2}$, respectively, and the characteristic BEs of 159.1 and 164.4 eV could be ascribed
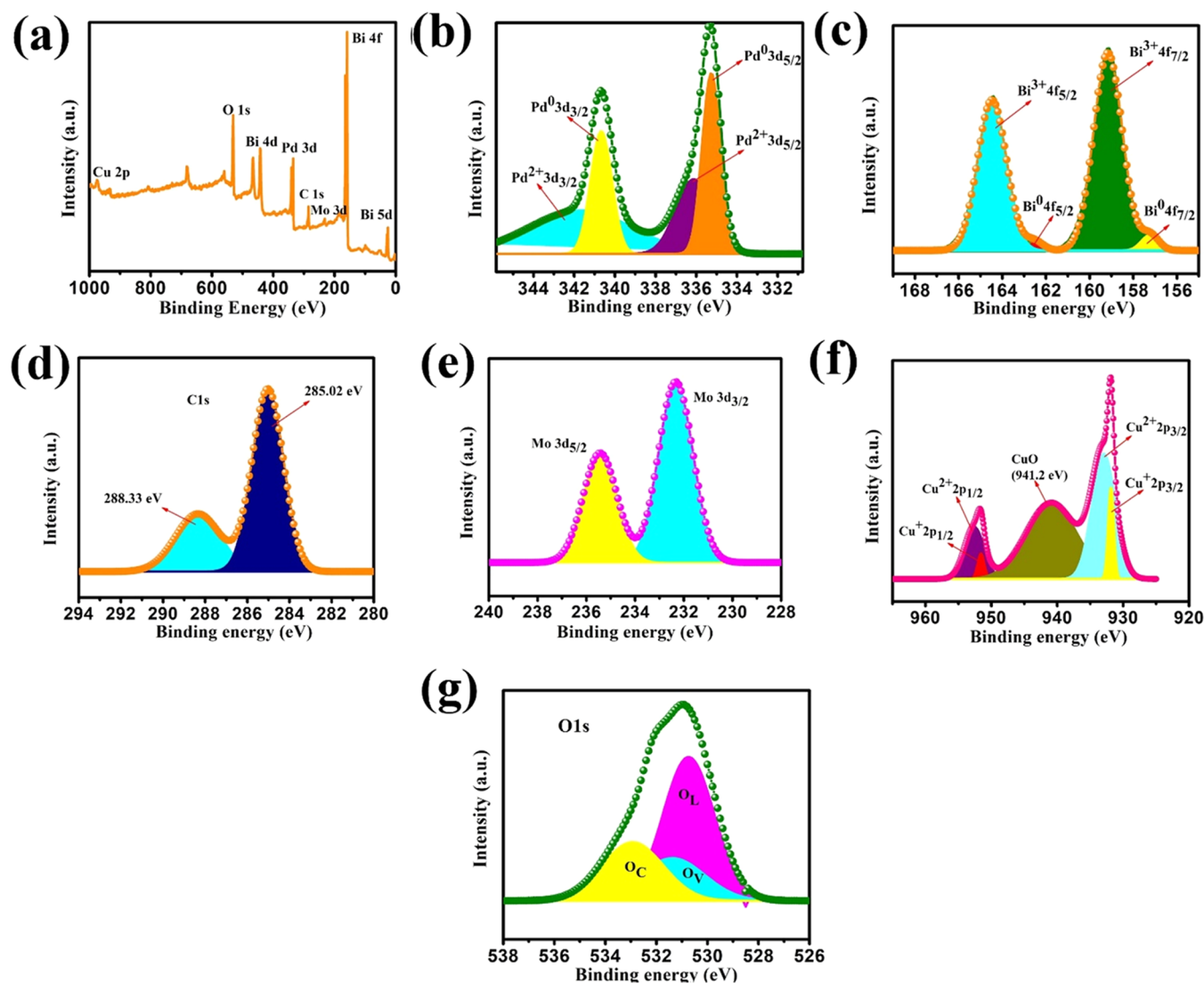
Figure 4. XPS spectra of the Pd/Bi$_2$MoO$_6$-Bi$_2$O$_2$CO$_3$-CuO composite: (a) survey scan, (b) Pd 3d, (c) Bi 4f, (d) C 1s, (e) Mo 3d, (f) Cu 2p, and (g) O 1s.

to the Bi^{3+} 4f$_{7/2}$ and 4f$_{5/2}$, respectively.[62,63] Figure 4d reveals the BEs of C 1s centered at 285 and 288.3 eV; the first one is the adventitious carbon peak used for calibration and the second peak may be ascribed to the carbon of carbonate in Bi$_2$O$_2$CO$_3$.[64] The two typical peaks (Figure 4e) located at BEs of 232.4 and 235.5 eV should be assigned to 3d$_{5/2}$ and 3d$_{3/2}$ of Mo^{6+} states of Bi$_2$MoO$_6$, respectively.[65] The CuO species in the Pd/Bi$_2$MoO$_6$-Bi$_2$O$_2$CO$_3$-CuO composite can be easily recognized (Figure 4f) by its main peaks of Cu 2p$_{3/2}$ and Cu 2p$_{1/2}$ located at 933 and 952.6 eV, respectively. The characteristic satellite peak at 940 eV is due to the presence of Cu^{2+} and is unique for Cu^{II}O nanoparticles. Indeed, two small peaks fitted at 931.8 and 951.6 eV are due to Cu 2p$_{3/2}$ and Cu 2p$_{1/2}$ of Cu$^+$, respectively.[66−68] The deconvoluted O1s spectrum is presented in Figure 4g, and it shows the three main peaks with BEs of 530.7 (O$_L$), 531.4 (O$_V$), and 532.9 (O$_C$) eV and one small peak at the BE of 528.4 eV. This is due to the multiple oxygen atmospheres. The O$_L$ peak is the characteristic lattice oxygen of Bi−O, Cu−O, and Mo−O in the BM-BOCC catalyst. The peak O$_V$ is attributed to the oxygen defects in the metal oxide matrix,[69,70] and the peak O$_C$ is related to surface hydroxyl or water molecules adsorbed on the metal oxide

surfaces.[71] The concentration of the oxygen defect is estimated by comparing the relative peak area ratio of O$_L$, O$_V$, and O$_C$ peaks. The integrated peak area of O$_L$, O$_V$, and O$_C$ is found to be 53.6, 20.2, and 26.2%, respectively. Therefore, oxygen defects in the Pd/BM-BOCC catalyst are helpful to the photo-electrocatalytic activity of ethanol oxidation under visible light illumination.[70]

In Figure 5, TEM, HRTEM, and SAED images of Pd/Bi$_2$MoO$_6$-Bi$_2$O$_2$CO$_3$, Pd/CuO, and Pd/ Bi$_2$MoO$_6$-Bi$_2$O$_2$CO$_3$-CuO heterostructures are presented. The TEM image of Pd/BM-BOC as shown in Figure 5a displays spherical black dots of Pd nanoparticles homogeneously spread over the Bi$_2$MoO$_6$-Bi$_2$O$_2$CO$_3$ surface. In Figure 5b, the HRTEM image of Pd/BM-BOC shows the highlighted lattice fringe of 0.23 nm, 0.29 nm, and 0.31 nm, and the SAED profile (Figure 5c) also indicates the presence of (111), (161), and (131) planes for Pd, Bi$_2$O$_2$CO$_3$, and Bi$_2$MoO$_6$, respectively.[39,72] Figure 5d reveals the formation of CuO nanoplates with spherical metallic Pd on its surface. The HRTEM (Figure 5e) and SAED (Figure 5f) identify the interplanar distance of 0.23 and 0.27 nm, which can be accredited to the (111) and (110) planes of Pd and CuO, respectively.[73] In Figure 5g, it was
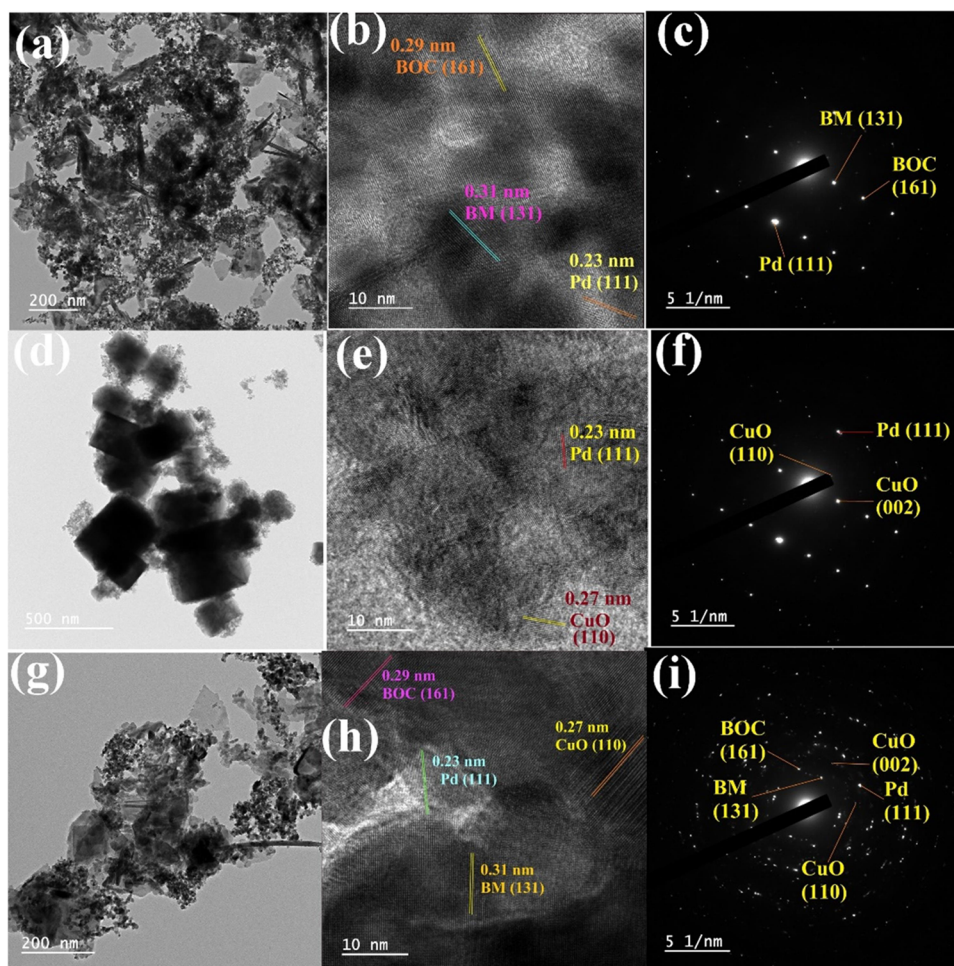
Figure 5. TEM images, HRTEM images, and SAED of Pd/ Bi_2MoO_6-$Bi_2O_2CO_3$ (a, b, c), Pd/CuO (d−f), and Pd/ Bi_2MoO_6-$Bi_2O_2CO_3$ -CuO (g−i) catalysts, respectively.

found that spherical Pd of an average size of 2−3 nm was spread uniformly over the whole surface of the Bi_2MoO_6-$Bi_2O_2CO_3$-CuO heterostructure.

The interplanar spacings of 0.23, 0.27, 0.29, and 0.31 nm are ascribed to the (111), (110), (161), and (131) planes of cubic Pd, monoclinic CuO, and orthorhombic $Bi_2O_2CO_3$ and Bi_2MoO_6 as obtained from the HRTEM image of Pd/BM-BOCC in Figure 5h, respectively, and the SAED pattern of Pd/BM-BOCC (Figure 5i) is properly fitted with XRD data. Therefore, the TEM images support the successful formation of binary, ternary, and quaternary heterojunctions.

The optical properties of the synthesized BM/BOC, Pd/BM/BOC, CuO, Pd/CuO, and Pd/ Bi_2MoO_6-$Bi_2O_2CO_3$-CuO (Pd/BM/BOCC) nanocatalysts were investigated by UV−vis absorption and photoluminescence (PL) spectroscopy. The absorption spectra of the as-prepared catalysts (Figure S4a) exhibit that the introduction of Pd and CuO to the Bi_2MoO_6-$Bi_2O_2CO_3$ nanocatalyst shifts the wavelength of absorption in the red direction. When Pd is doped with the pure CuO and Bi_2MoO_6-$Bi_2O_2CO_3$ junction, a wide absorption band region is observed from 300 to 700 nm. The optical direct band gap energy (E_g) of the synthesized catalysts can be determined from the Tauc equation[74,75] $(\alpha h\nu)^2 = A (h\nu - E_g)$, where α, $h\nu$, E_g, and A are the absorption coefficient, photon energy, optical band gap, and a constant, respectively, as presented in Figure S4b and Table 1. According to the plot, the band gap

Table 1. Elemental Compositions and Their Chemical States of the Synthesized Pd/Bi_2MoO_6-$Bi_2O_2CO_3$-CuO Heterojunction from XPS Study

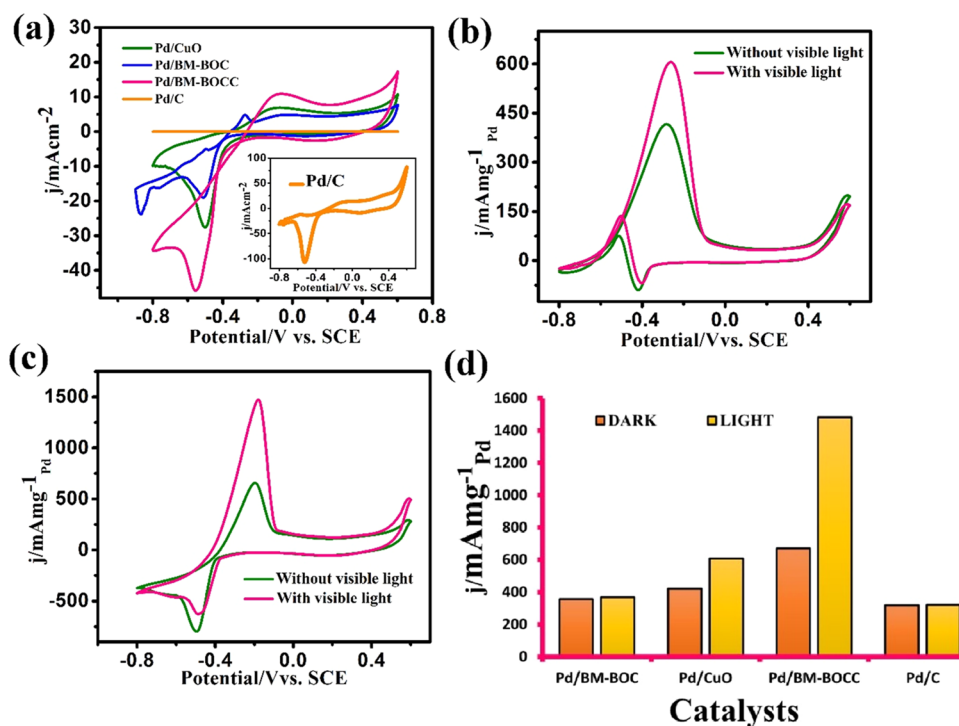| element	peak	position (B.E) eV
Bi 4f	Bi^{3+} $4f_{7/2}$	159.1
	Bi^{3+} $4f_{5/2}$	164.4
	Bi^0 $4f_{7/2}$	157.2
	Bi^0 $4f_{5/2}$	162.5
C 1s		285
	C for CO_3^{2-}	288.3
Pd 3d	$Pd^0 3d_{5/2}$	335.2
	$Pd^0 3d_{3/2}$	340.6
	$Pd^{2+}3d5_{/2}$	336.1
	$Pd^{2+}3d_{3/2}$	341.7
Mo 3d	$Mo^{6+}3d_{5/2}$	232.4
	$Mo^{6+}3d_{3/2}$	235.5
Cu 2p	Cu^{2+} $2p_{3/2}$	933
	Cu^{2+} $2p_{1/2}$	952.6
	Cu^{2+}	940
	Cu^+ $2p_{3/2}$	931.8
	Cu^+ $2p_{1/2}$	951.6
O 1s	O_L	530.7
	O_V	531.4
	O_C	532.9

Figure 6. (a) CV curves of Pd/BM-BOC, Pd/CuO, Pd/BM-BOCC, and Pd/C (lower inset) electrodes in the N_2-saturated solution of 1 M NaOH solution at 50 mV s^{-1}. Typical CV curves (mass activity) of the synthesized (b) Pd/CuO and (c) Pd/BM-BOCC electrodes in the N_2-saturated 1 M EtOH + 1 M NaOH solution with and without visible light irradiation at 50 mV s^{-1}, test temperature: 25 °C (d) Histogram profile of various catalysts in terms of mass-normalized peak current density.

values are 2.80 and 1.81 eV for Bi_2MoO_6 and Pd/CuO catalysts, respectively, and three values of 1.61, 2.18, and 2.40 eV are for the Pd/Bi_2MoO_6-$Bi_2O_2CO_3$ catalyst (the first one concerning CuO,[76] the second is for Bi_2MoO_6,[77] and last value is for $Bi_2O_2CO_3$[78]). Clearly, the gradual decrease of the band gap of Bi_2MoO_6 and CuO in the Pd/Bi_2MoO_6-$Bi_2O_2CO_3$-CuO quaternary heterojunction indicates enhanced visible light absorption as well as photo-electrocatalytic activity of the EOR.

The potentials of E_{CB} and E_{VB} of p-CuO, n-$Bi_2O_2CO_3$, n-Bi_2MoO_6, and p−n−n heterojunction (Pd/BM-BOCC) have been calculated by the following equations

$$E_{CB} = \chi - E^c - 0.5\,E_g$$

$$E_{VB} = E_{CB} + E_g$$

where E^c and χ are the free electronic energy on the NHE scale (about 4.5 eV) and absolute electronegativity, respectively, and E_{CB} and E_{VB} are the conduction and valence band edge potential, respectively. The χ values (obtained from the literature) for Bi_2MoO_6, $Bi_2O_2CO_3$, and CuO are about 6.13, 6.35, and 5.89 eV, respectively.[58,79,80] Based on the above-mentioned equations, the top of VBs lies at 2.72, 3.05, and 2.20 V and the corresponding bottom of CB values is 0.54, 0.65, and 0.59 V, respectively, for Bi_2MoO_6, $Bi_2O_2CO_3$, and CuO in the Pd/BM-BOCC composite.

The photoexcited electron−hole pair transfer and separation efficiency were elucidated by PL spectra in Figure S4c. All the spectra were achieved by excitation at 280 nm and show an emission peak at 399 nm. The emission intensity follows the order Pd/ Bi_2MoO_6-$Bi_2O_2CO_3$ −CuO <Pd/CuO <Pd/ Bi_2MoO_6-$Bi_2O_2CO_3$ <Bi_2MoO_6-$Bi_2O_2CO_3$. The decrease of PL intensity in Pd/BM-BOCC infers the diminished

recombination and enhancement of charge separation[14,16] of photogenerated e$^-$−h$^+$ pairs, which might be due to the formation of heterojunctions among Bi_2MoO_6, $Bi_2O_2CO_3$, CuO, and Pd.

2.2. Photo-electrocatalytic Activity toward EtOH Oxidation. The cyclic voltammetry (CV) curves of Pd/Bi_2MoO_6-$Bi_2O_2CO_3$, Pd/CuO, and Pd/Bi_2MoO_6-$Bi_2O_2CO_3$-CuO catalysts obtained using 1 M NaOH solution are exhibited in Figure 6a, and the clear image of the Pd/C catalyst is given in the inset figure. In the forward scan of Pd nanoparticles (inset figure), the three peaks found around −0.570, −0.113, and 0.348 V are ascribed to the desorption of Pd-H and formation of Pd−OH and Pd−O, respectively. The well-defined peak at ca −0.514 V in the backward scan denotes the reduction process from PdO to Pd. From Figure 6a, it is clear that all the Pd-doped binary and ternary catalysts exhibit typical M−OH$_{ads}$ and M−O peaks. The higher current density of the Pd/ Bi_2MoO_6-$Bi_2O_2CO_3$-CuO (Pd/BM-BOCC) catalyst for the formation of M−OH$_{ads}$ and M−O reveals more OH$^-$ adsorption on its surface. The OH$^-$ ion adsorption peak is observed at a very negative potential (ca −0.274V) for the Pd/ Bi_2MoO_6-$Bi_2O_2CO_3$ catalyst compared to the quaternary catalyst, indicating facile OH$^-$ ion adsorption of Pd in the presence of the Bi surface.

The number of electrochemical active sites in the surface of catalysts is an essential parameter that determines the electrocatalytic activity of catalysts. The electrochemical active surface area (ECSA) of the synthesized catalysts is calculated from the adsorbed monolayer of the PdO reduction peak in the cyclic voltammetry measurement of 1 M NaOH solution in the range between +0.2 and −0.8 V/SCE at a scan rate of 0.05 Vs^{-1} (exhibited in Figure 6a) using the following equation

Table 2. Summarization Table of Photo-electrocatalytic Performance Parameters toward the EOR in Alkali Including Band Gap and ECSA of the As-Prepared Nanocatalysts

catalysts	band gap (Eg)/eV	dark conditions			ECSA from CV studies (m^2g^{-1})	under illumination of visible light		
		forward peak potential (V)	backward peak potential (V)	forward peak current density in dark ($mAmg^{-1}$ of Pd)		forward peak potential (V)	backward peak potential (V)	forward peak current density in light ($mAmg^{-1}$ of Pd)
Pd/BM-BOC	2.37, 2.53	−0.233	−0.439	356.2	9.17	−0.220	−0.463	368.3
Pd/CuO	1.81	−0.283	−0.436	420.9	11.63	−0.265	−0.428	608.3
Pd/BM-BOCC	1.61, 2.18, 2.40	−0.191	−0.495	670.5	21.43	−0.178	−0.483	1482.5
Pd/C		−0.218	−0.374	318.4	0.243	−0.214	−0.372	321.5

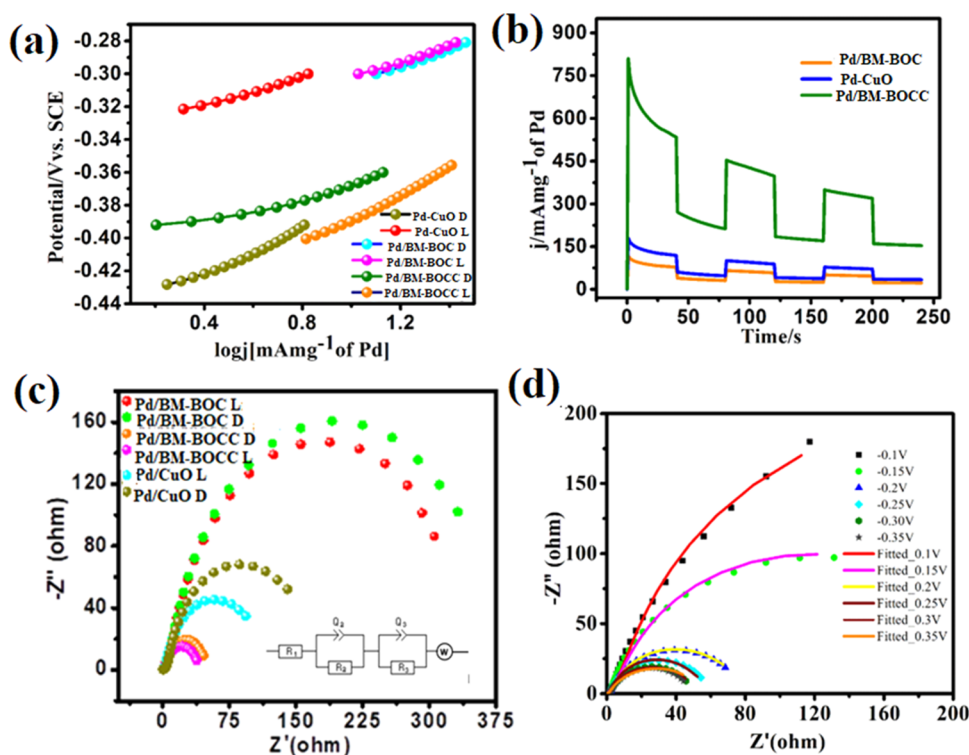**Figure 7.** (a) Tafel plots of the synthesized Pd/BM-BOC, Pd/CuO, and Pd/BM-BOCC electrodes obtained from CV experiments operated at 1 mV s^{-1} scan rate in the presence and absence of light using 1 M EtOH + 1 M NaOH solution. (b) Transient photocurrent responses of the synthesized catalysts immersed in 1 M EtOH + 1 M NaOH solution under visible light illumination recorded at −0.3 V. (c) Nyquist plots of the constructed electrodes using nitrogen-saturated alkaline ethanol solution at −0.3 V with and without visible light exposition in the range of 0.1−100 Hz and the lower inset represents the equivalent circuit for fitting impedance data. (d) Nyquist plots of the Pd/BMBOCC quaternary catalyst at various potentials in the same solution.

$$\text{ECSA} = \frac{S \times 0.12}{v \times 0.405 \times m}$$

where S is the PdO reduction peak area in cyclic voltammetry, v is the scan rate, 0.405 (mCcm^{-2}) is a constant defined as the charge required for the reduction of the monolayer of oxide on Pd, 0.12 cm^2 is the surface area of the electrode, and m is the loading amount of the catalyst.[11,81] The ECSA (m^2g^{-1}) values of the prepared electrodes are in the order Pd (0.243) <Pd/BM-BOC (9.17) <Pd/CuO (11.63) <Pd/BM-BOCC (21.43), indicating the highest ECSA of the quaternary heterojunction catalyst. Thus, the presence of oxide materials and particularly CuO increases the ECSA of the catalyst system studied.

The electrocatalytic and photo-electrocatalytic activities of the as-prepared electrodes toward the ethanol oxidation reaction (EOR) were assessed by the CV procedure in 1 M ethanol + 1 M NaOH solution with the absence and presence

of visible light at a sweep rate 50 mV s^{-1} and depicted in Figure 6b and c, respectively.

The peak potential, mass-normalized current density, and other related parameters are summarized in Table 2. The forward peak and backward peak (E_{pf} and E_{pb}) originated in the range from −0.25 to −0.28 V and −0.43 to −0.51 V, respectively. The oxidation peak can be ascribed to the oxidation of freshly chemisorbed ethanol, and the reverse peak is primarily due to the elimination of residual carbonaceous intermediates generated in the anodic scan for incomplete oxidation. The reduction peak of the Pd/BM-BOCC catalyst was observed at a lower potential (E_{pr}, at ca −0.48 V), indicating that PdO of the quaternary catalyst is more easily reduced compared to binary catalysts. It is worth mentioning that the forward oxidation peak potential of all electrocatalysts under light irradiation shifts to a more positive direction compared to the peak potential in the dark. This may be assumed that poisonous intermediates which oxidized in higher
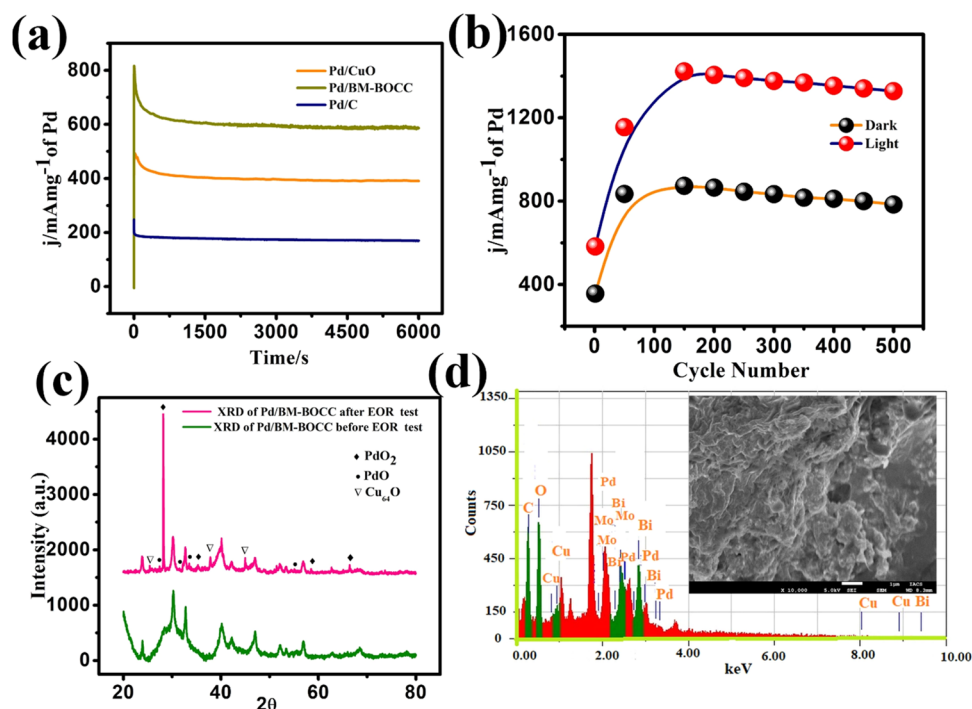
Figure 8. (a) Current density−time profiles of Pd/CuO/C, Pd/BM-BOCC/C, and Pd/C electrodes at a fixed potential of −0.3 V up to 6000 s under visible light illumination. (b) Electrocatalytic stability test from multiple CV cycling of Pd/BM-BOCC/C electrodes with and without visible light in nitrogen-saturated solution of 1 M EtOH + 1 M NaOH at 50 mV s^{-1}. (c) PXRD pattern of the quaternary catalyst before and after the five hundred cycling test under visible light irradiation. (d) EDX spectrum and FESEM (inset) of the used catalyst.

potential become further oxidized in the presence of visible light.

The typical CV profiles of the modified Pd/CuO and Pd/BMBOCC electrodes in 1 M ethanol + 1 M NaOH solution in dark and light conditions are exhibited in Figure 6b and c, respectively. It is noticed that the forward peak current density (I_f, mA mg^{-1} of Pd) for the EOR under dark conditions follows the order: Pd/C (318.4) <Pd/BM-BOC (356.2) <Pd/CuO (420.9) <Pd/BM-BOCC (670.5), and light illumination obeys the same order: Pd/C (321.5) <Pd/BM-BOC (368.3) <Pd/CuO (608.3) <Pd/BM-BOCC (1482.5). The mass activities of Pd/C and Pd/BM-BOC catalysts are shown in Supporting Figure S5.

Our best quaternary heterojunction catalyst, Pd/BM-BOCC, exhibits peak current density in visible light, which is 2.43, 4, and 4.6 times higher than that of Pd/CuO, Pd/BM-BOC, and Pd/C catalysts, respectively. Only small improvements in peak current density were observed under visible light illumination; nearly 2.21 times greater current is obtained than that in the dark. Figure 6d and Table 2 show the superiority of catalytic activity (maximum mass-normalized current density) of the quaternary catalyst achieved in both dark and light conditions. The significant increase in EOR current density is ascribed to the synergistic effects of electro- and photocatalytic properties of Pd/ Bi$_2$MoO$_6$-Bi$_2$O$_2$CO$_3$-CuO. Moreover, the photo-electrocatalytic oxidation of our synthesized quaternary catalyst is compared with other Pd-based materials reported earlier in Table S1. This clearly reveals that our synthesized catalyst exhibits much better EOR activity in visible light.

Tafel plots of the synthesized electrodes are fitted in the presence and absence of visible light and displayed in Figure 7a. It is noticed from the figure that the quaternary catalyst Pd/BM-BOCC has the smallest Tafel slope value (90 mV dec^{-1})

under visible light compared to other electrocatalysts. This indicates that the quaternary electrocatalyst is more efficient in charge transfer kinetics in the EOR at the equilibrium region under visible light illumination.[2,4,10,11]

To measure the photoelectric properties of the synthesized nanocatalysts, the photocurrent response measurement of Pd/BM-BOC, Pd/CuO, and Pd/BM-BOCC was performed at −0.3 V potential vs SCE by interrupting visible light with a duration of 50s as shown in Figure 7b. The photocurrent response diminished quickly once the light is switched off.[14,25,26] The figure reveals the higher responsive photocurrents of the Pd/BM-BOCC quaternary catalyst owing to enhanced light absorption and better interfacial charge transfer[54,82] of the quaternary catalyst during ethanol photooxidation.

EIS spectroscopy was employed to inspect the charge transfer kinetics of electrode reactions. Figure 7c exhibits the Nyquist plots of Pd/BM-BOC, Pd/CuO, and Pd/BM-BOCC electrodes immersed in 1 M EtOH + 1 M NaOH solution measured at a potential of − 0.3 V under dark and light conditions. It shows that the semicircle diameter of Pd/BM-BOCC electrodes is the smallest corresponding to the electrode made using Pd/BM-BOC and Pd/CuO. Again, these electrodes on light exposure further decreased the diameter of the arc. This result indicates that light irradiation made a marked improvement in interfacial charge transport and enhancement of e$^-$−h$^+$ separation[14,16,83] in the n−n and n−p junction of the quaternary composite. The role of Bi$_2$MoO$_6$-Bi$_2$O$_2$CO$_3$ in photo-electrocatalytic ethanol oxidation is the enhanced separation and transfer of photogenerated electron−hole pairs.[22] The potential dependence interpretation of the Nyquist plot for the EOR on the quaternary catalyst Pd/BM-BOCC was also executed at different constant
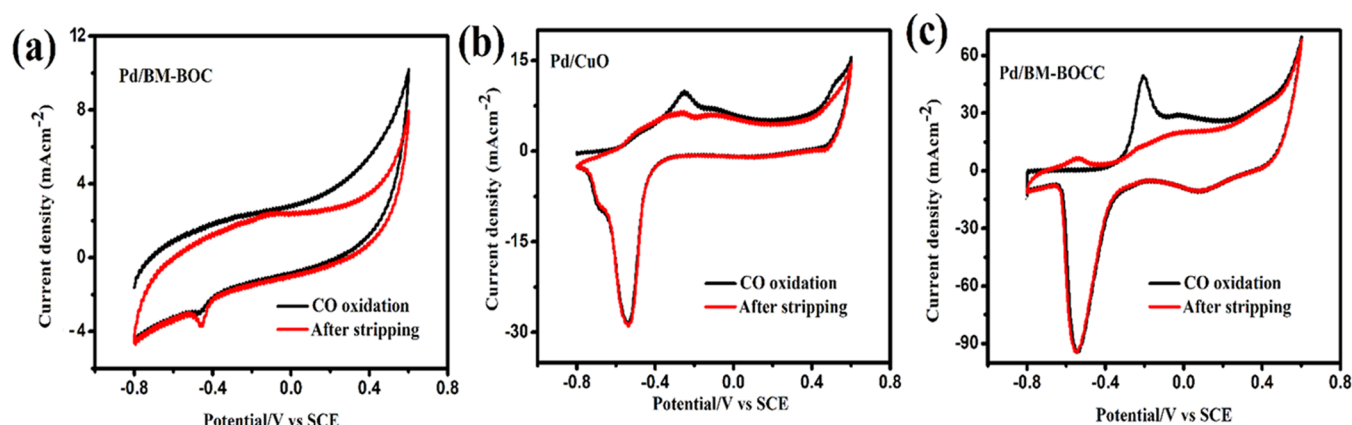
Figure 9. CO oxidation and stripping of (a) Pd/BM-BOC heterojunction, (b) Pd/CuO heterojunction, and (c) Pd/BM-BOCC heterojunction in 1 M NaOH solution at a scan rate 50 mV s^{-1} and 25°C in dark conditions. The black line represents the first scanning cycle, and the red line represents the second scanning cycle.

potentials in the range of −0.1 to −0.35 V under light illumination (Figure 7d). The Nyquist diameter continuously increases with increasing potential from −0.35 to −1.0 V. This is due to the carbonaceous intermediate's species poisoning the catalyst at a higher potential.[14,16,51,84]

2.3. Stability of Photo-electrocatalysts. The long-term electrocatalytic stability of the synthesized catalysts was judged by chronoamperometric measurement at a potential of −0.3 V for 6000 s and multiscan CV experiment of the quaternary heterojunction electrode up to 500 cycles in the potential range from −0.8 to + 0.6 V at a scan rate of 50 mV s^{-1} with and without visible light as shown in Figure 8a,b respectively.

Figure 8a displays the CA profile of Pd/CuO, Pd/BM-BOCC, and Pd/C electrodes in the alkaline ethanol solution under visible light illumination.

CA study manifests greater quasi-stationary current density of the quaternary heterostructure electrode (Pd/BM-BOCC) after 6000 s of operation, which is 1.5 and 3.4 times greater than that of Pd/CuO (392.4 mA mg^{-1}Pd) and Pd/C (172.3 mA mg^{-1}Pd) catalysts, respectively, indicating that the addition of bismuth subcarbonate, bismuth molybdate, and CuO as supports to the principal catalyst Pd facilitates the EOR by the removal of the adsorbed CO intermediates and exhibits excellent stability and enhanced synergistic effect for photo-electrocatalytic ethanol oxidation under visible light.[48,85,86]

Figure 8b presents the regular increase of forward peak current density of the Pd/BM-BOCC/C electrode up to 150 cycles and achieves a maximum current of 882.2 and 1443.2 mA mg^{-1}Pd in the dark and light, respectively. Then, the peak current density decreases sluggishly and the stability test shows that the quaternary catalyst loses only 9.8 and 7.7% of its maximum current density after 500 cycles CV in the dark and light, respectively, indicating that light energy is more beneficial in establishing stability.

To understand the mystery of the photo-electrocatalytic activity and stability of the quaternary catalyst, PXRD was carried out after the 500th cycle CV operation of the catalyst in the presence of visible light and surface morphology of the used catalyst after the CV test was characterized by FESEM.

The PXRD profile (Figure 8c) shows that the main phases of the catalyst remain unaltered and all elements are found in EDX spectra (Figure 8d) as mentioned earlier. However, along with these phases, new peaks of PdO$_2$, PdO, and Cu$_{64}$O phases

were generated during the EOR test under visible light. The peaks 2θ (/degree) at 28.15, 35.18, 58.4, and 66.4 correspond to the (110), (101), (220), and (221) planes of hexagonal PdO$_2$ (JCPDS 376377), respectively. The peaks 2θ (/degree) at 27.31 and 31.64 are assigned to the (111) and (200) planes of cubic PdO (JCPDS 655261) and the peaks 33.64 and 54.60 arise from the (002) and (112) tetragonal PdO plane (JCPDS 850624), respectively, and some very small peaks around 2θ (/degree) at 25.34, 35.43, 37.86, and 44.88 were found, which may be attributed to the (123), (141), (410), and (008) planes of orthorhombic Cu$_{64}$O, respectively. (JCPDS 771898). During a long time of photo-electrochemical oxidation process, Pd is oxidized to PdO$_2$ and PdO and CuO forms lower oxygen content copper oxide, Cu$_{64}$O. This infers that CuO favors the formation of PdO and oxygen released by the PdO-to-Pd conversion can oxidize ethanol, and this might be the reason for the initial growth of current density.[20,86,87] The small reduction of current density after 500 cycles of CV in visible light is due to the deactivation and poisoning of the catalyst surface. The previous literature investigated that the formation of ultrathin layer PdO and PdO/PdO$_2$ on the Pd metal surface significantly enhances EOR activity in alkali medium.[13,88,89] Krittayavathanum et al. reported that the deposition of the thin PdO layer on Pd easily binds ethanol and its intermediates, leading to high current density, and the decline in current density with increasing cycling is due to the higher amount of PdO deposition on the Pd surface, activity similar to that of the bulk PdO.[88] Therefore, our observations agree well with the previous results.[13,20,86−89]

Figure S6a,b demonstrate the morphology of the quaternary catalyst before and after the cycling test at different magnifications. From the figures, it is found that little change in the overall morphology and the gaps and holes between the layer and particles are reduced in the used catalyst. The particles are relatively more interconnected in the lattice, which may provide multiple conductive paths for an easier flow of electrons.[90] Moreover, the interconnection may lead to an effective increase in particle size, causing less effective surface area for further ethanol oxidation. This might be the cause of the slight reduction of current density in higher cycling.

The CO antipoisoning test was performed by purging the CO gas in 1 M NaOH solution as exhibited in Figure 9. In this figure, the first cycle appears for the CO oxidation peak, and in the second scan, this peak disappears because of the complete
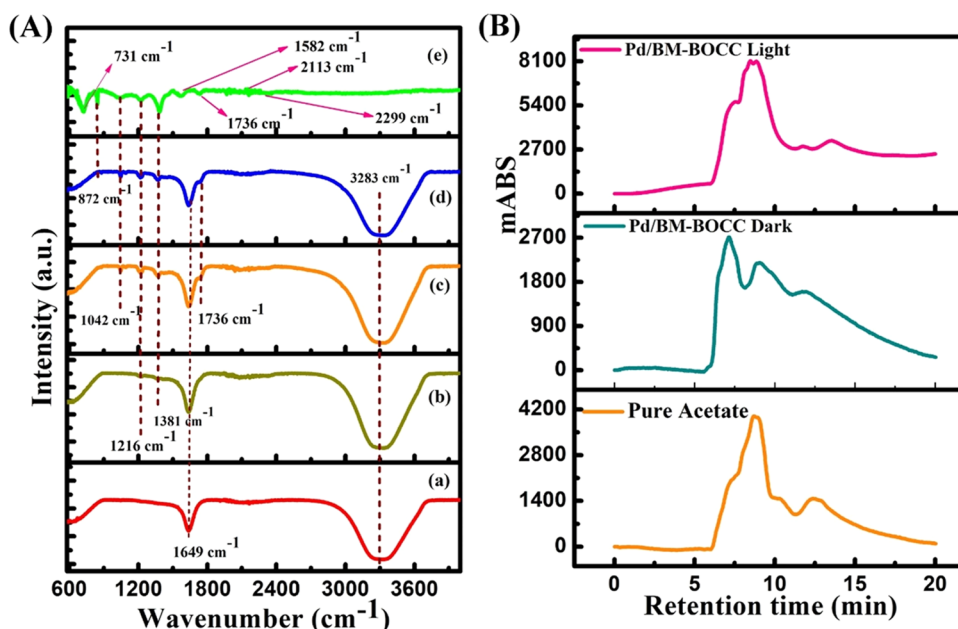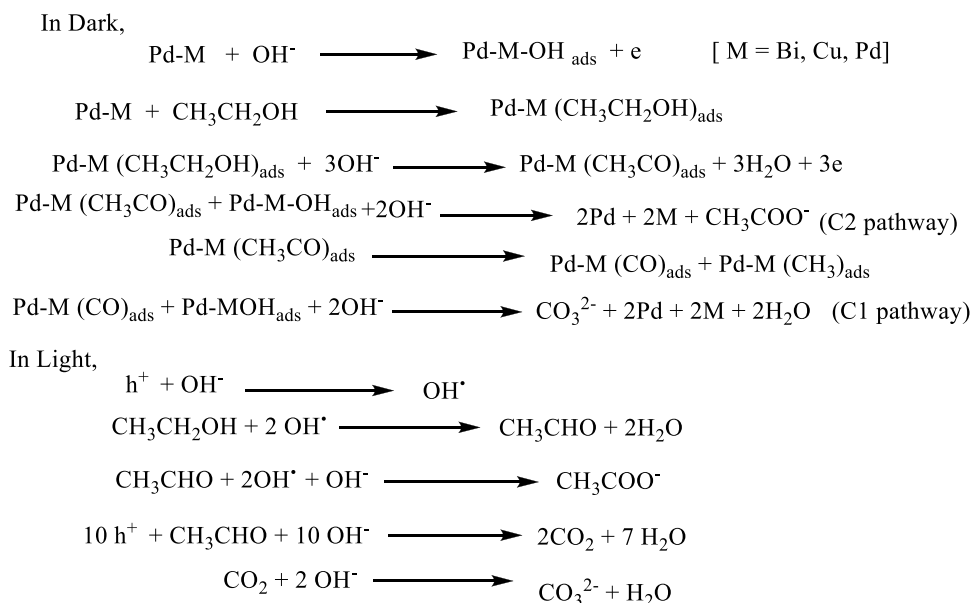
Figure 10. (A) FTIR spectra of (a) EtOH before oxidation and (b) pure acetate. EtOH after electrooxidation in alkali by (c) Pd/BM-BOC heterojunction, (d) Pd/CuO heterojunction, and (e) Pd/BM-BOCC heterojunction. (B) HPLC profiles of ethanol oxidation products in alkali using Pd/BM-BOCC catalysts in the dark and light and known concentration of acetate.

Scheme 2. Electrocatalytic and Photo-electrocatalytic Oxidation of Ethanol on the Synthesized Heterojunction in the Dark and Light Conditions

In Dark,

$$Pd\text{-}M + OH^- \longrightarrow Pd\text{-}M\text{-}OH_{ads} + e \qquad [M = Bi, Cu, Pd]$$

$$Pd\text{-}M + CH_3CH_2OH \longrightarrow Pd\text{-}M(CH_3CH_2OH)_{ads}$$

$$Pd\text{-}M(CH_3CH_2OH)_{ads} + 3OH^- \longrightarrow Pd\text{-}M(CH_3CO)_{ads} + 3H_2O + 3e$$

$$Pd\text{-}M(CH_3CO)_{ads} + Pd\text{-}M\text{-}OH_{ads} + 2OH^- \longrightarrow 2Pd + 2M + CH_3COO^- \text{ (C2 pathway)}$$

$$Pd\text{-}M(CH_3CO)_{ads} \longrightarrow Pd\text{-}M(CO)_{ads} + Pd\text{-}M(CH_3)_{ads}$$

$$Pd\text{-}M(CO)_{ads} + Pd\text{-}MOH_{ads} + 2OH^- \longrightarrow CO_3^{2-} + 2Pd + 2M + 2H_2O \quad \text{(C1 pathway)}$$

In Light,

$$h^+ + OH^- \longrightarrow OH^\bullet$$

$$CH_3CH_2OH + 2OH^\bullet \longrightarrow CH_3CHO + 2H_2O$$

$$CH_3CHO + 2OH^\bullet + OH^- \longrightarrow CH_3COO^-$$

$$10h^+ + CH_3CHO + 10OH^- \longrightarrow 2CO_2 + 7H_2O$$

$$CO_2 + 2OH^- \longrightarrow CO_3^{2-} + H_2O$$

removal of carbon monoxide from the catalyst surface.[16,91] The peak potential of CO oxidation is −0.126, −0.253, and −0.208 V (vs SCE) for Pd/BM-BOCC, Pd/CuO, and Pd/BM-BOCC catalysts, respectively. The more negative shift of the CO oxidation peak potential of Pd/CuO indicates that CuO doping on Pd and Pd/BM-BOC catalysts can easily remove the CO intermediates during the EOR by the following reaction[87]

$$CO_{ads} + OH_{ads} \rightarrow CO_2 + H_2O$$
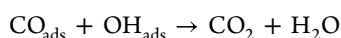
The electrochemical active surface area (ECSA) was calculated from the CO stripping experiment by taking monolayer CO adsorption on Pd.[40] The ECSA of the quaternary catalyst Pd/BM-BOCC (29.4 m^{2}g^{-1}) is 2.1 and 3

times greater than that of Pd/CuO and Pd/BM-BOC, respectively. The highest ECSA and highest peak current density toward CO oxidation of the quaternary catalyst reveal better CO tolerance and superior EOR activity.[49]

2.4. Identification of Ethanol Oxidation Products. FTIR spectra of ethanol in alkali before and after oxidation by the synthesized nanocatalysts are exhibited in Figure 10A. For comparison, the FTIR spectrum of pure acetate is also characterized. In Figure 10 A, ethanol in alkali (before oxidation) shows a broad peak in the range of 3200−3400 cm^{-1}, revealing the −OH group of ethanol, and the peak 1649 cm^{-1} is ascribed to the presence of the −C=O group of acetate.[11,15] The peak at 1736 cm^{-1} is due to the −C=O

stretching (without H bonding), and the peaks at 1216 and 1049 cm^{-1} may be attributed to $-OH$ and $-C-OH$ stretching of ethanol, respectively.[12] With ethanol oxidation in alkali by the quaternary catalyst, spectra (e) in Figure 10A exhibit the peak at 1386 and 1582 cm^{-1}, which is assigned to the symmetric and asymmetric stretching of the $-O-C-O$ group of acetate, respectively. The bands at 2113 and 2299 cm^{-1} are ascribed to the CO vibration and asymmetric stretching vibration of CO_2, respectively,[21,47,92] and the peaks observed at 872 and 731 cm^{-1} are from carbonate.[11] Most of the peaks in portion (e) of Figure 10A reveal the $-C-C$ bond rupture during the EOR. Therefore, it is concluded that more acetate is formed in Pd/BM-BOC and Pd/CuO binary catalysts and more carbonate is formed from the quaternary catalyst as shown in Scheme 2.

The HPLC profiles of ethanol oxidation products obtained after 6000 s of CA at a fixed potential of -0.3 V[11,16,51] using quaternary Pd/BM-BOCC catalysts under dark and illuminated conditions are exhibited in Figure 10B, and the retention time of the pure acetate compound is also drawn using its known concentration for evidence. The retention tenures of 7.12 and 8.59 min refer to the formation of carbonate and acetate, respectively. The HPLC profile shows significantly enhanced acetate and carbonate production when the quaternary catalyst is irradiated under visible light. The huge amount of electrooxidation species confirms the greater extent of the electrocatalytic oxidation process of ethanol under irradiation compared to that in the dark.

2.5. Mechanism of Ethanol Oxidation. In the dark, ethanol initially adsorbs on Pd-M surfaces; then, stepwise dehydrogenation produces acetyl (adsorbed) intermediates. On the other hand, Pd-M-OH$_{ads}$ is produced by hydroxylation on Pd-M, which combines with acetyl intermediates to give the partial oxidation product of EOR, i.e., acetate in alkali by the C2 pathway.[2,4,10] In the poisoning pathway, CH_3CO_{ads} decomposes to give carbonate, with the complete oxidation of the EOR with the rupture of the $C-C$ bond by the C1 pathway shown in Scheme 2[15,87,89,93,94]

In light, an enhanced EOR mechanism was suggested, which is schematically exhibited in Figure 11. This reveals that the n-Bi_2MoO_6 (BM) forms n−n junctions with n-type $Bi_2O_2CO_3$ (BOC) and p-type CuO produces p−n junctions with $Bi_2O_2CO_3$.[95] At the BM−BOC junction, the excited electrons flow from the CB of BM to the CB of BOC, and

at the same time, holes in the VB of BOC go to the VB of BM. At the BOC/CuO junction, on the other hand, the photoexcited electrons transfer from the CB of CuO to BOC and holes transfer from BOC to CuO under light illumination[14,16,51,91] Thus, the formation of n−n and n−p heterojunctions significantly increases the separation of photoexcited e$^-$−h$^+$ and thereby interfacial charge transfer efficiency.[96,97] In the mechanism, the excited electrons are accumulated in the CB of BOC via noble metal Pd, making them available for ethanol electrocatalytic oxidation through the formation of OH$^\bullet$ (H$_2$O + e = OH$^\bullet$),[75,76] and in the opposite direction, holes are deposited to the VB of BM or CuO from the VB of BOC, which reacts with the OH$^-$ ion to produce OH$^\bullet$ radicals and decomposes ethanol to acetate and carbonate (also presented in Scheme 2).

3. CONCLUSIONS

We have successfully synthesized Pd/Bi_2MoO_6-$Bi_2O_2CO_3$, Pd-CuO, and Pd/Bi_2MoO_6-$Bi_2O_2CO_3$-CuO (Pd/BM-BOCC) novel heterojunctions without taking any additional carbon sources and used them as anode catalysts for the EOR in alkali in the presence and absence of visible light. XRD, FTIR, XPS, HRTEM, FESEM, and EDX mapping studies indicate the formation of the quaternary heterojunction and confirm strong coupling among palladium nanoparticles and Bi_2MoO_6-$Bi_2O_2CO_3$-CuO supports. The CV study reveals that the Pd/BM-BOCC catalyst exhibits better electrocatalytic activity in terms of forward peak current density than that of Pd/BM-BOC and Pd/CuO under visible light radiation. The lower semicircle arc of the quaternary electrode in the EIS measurement reveals the higher conductance of photo-generated charges in the junction. CA study exhibits excellent stability of the quaternary heterostructure electrode. Multiscan cycling of the CV experiment of the quaternary catalyst in light up to 500 cycles demonstrates the loss of only 7.7% of its maximum current density, also signifying excellent cycling stability for photo-electrooxidation of ethanol. The CO antipoisoning ability of the quaternary catalyst suggests that the presence of CuO in the composite facilitates the removal of the adsorbed CO$_{ads}$ during the EOR. PXRD of the used catalyst shows the formation of a small amount of $Cu_{64}O$ along with PdO and PdO_2, suggesting that the hydrogen produced in the dehydrogenation step of ethanol reacts with CuO to form oxygen-deficient species $Cu_{64}O$, and CuO induced the formation of PdO, and Pd conversion from PdO by the release of oxygen may oxidize ethanol to carbonate. Ex situ FTIR and HPLC studies illustrate the formation of acetate and carbonate as EOR products by C2 and C1 mechanisms, respectively. The study ensures more systematic stepwise development of EOR catalysts using oxide materials in future for the advent of photoassisted fuel cells.

4. EXPERIMENTAL SECTION

4.1. Materials. Bi (NO$_3$)$_3$·5H$_2$O, (NH$_4$)$_6$Mo$_7$O$_{24}$·4H$_2$O, Cu (NO$_3$)$_3$·3H$_2$O, NaOH, ethylene glycol, KCl, hydrazine hydrate, and ethanol were obtained from Merck without purification. 1% PdCl$_2$ (Arora Matthey Ltd.), Nafion (Sigma-Aldrich), and Millipore water were utilized throughout the experiments.

4.2. Synthesis of $Bi_2O_2CO_3$-Bi_2MoO_6. $Bi_2O_2CO_3$-Bi_2MoO_6 was synthesized by the hydrothermal method without using any additional carbon source. At first, a 25 mL
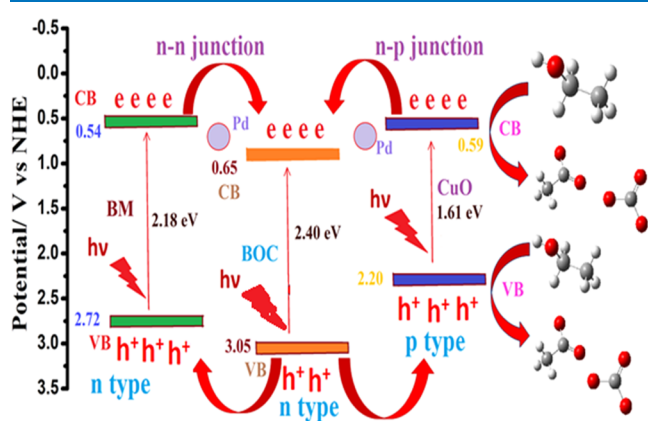

Figure 11. Plausible schematic mechanism for the ethanol oxidation reaction (EOR) on the Pd/BM-BOCC catalyst under visible light irradiation.

solution of 0.02 M Bi $(NO_3)_3 \cdot 5H_2O$ and 25 mL solution of 0.0015 M $(NH_4)_6Mo_7O_{24} \cdot 4H_2O$ were prepared in water and ethylene glycol solvent (1:1) separately and stirred for 0.5 h. Then, ammonium molybdate solution was mixed dropwise into the bismuth nitrate solution with the agitated conditions, and the pH of the whole solution is adjusted to 8. In order to make the suspension homogeneous, the mixture was vigorously stirred in magnetic stirring at 600 rpm for another 1 h. Then, the mixture was moved to a 50 mL Teflon-lined stainless-steel autoclave and kept at 160 °C for 10 h. The yellow-white powder was obtained with room temperature cooling, centrifugation (7000 rpm, 5 min), repeatedly washing with water and alcohol, and drying at 80 °C for 6 h. Finally, the powder was annealed at 400 °C for 2 h to form the $Bi_2O_2CO_3$-Bi_2MoO_6 (BM-BOC) composite.

4.3. Synthesis of CuO. CuO was prepared by the chemical precipitation method. At first, 25 mL of 0.1 M Cu $(NO_3)_3 \cdot 3H_2O$ solution (pH 5.06) was prepared in the mixed solvent water and ethylene glycol (1:1) and pH was adjusted to 12 by adding 1 M NaOH under stirring conditions. The mixture was vigorously stirred for 30 min and heated at 80 °C. Finally, a dark-brown precipitate was obtained after washing with ultrapure water and alcohol repeatedly and drying at 80 °C for 6 h.

4.4. Synthesis of $Pd/Bi_2O_2CO_3$-Bi_2MoO_6, Pd/CuO, and Pd/Bi_2MoO_6-$Bi_2O_2CO_3$-CuO Heterojunctions. At first, 0.609 g of prepared Bi_2MoO_6- $Bi_2O_2CO_3$ was sonicated in 100 mL of Millipore water for 2 h to form a 0.01 M suspension, A, and 0.241 g of Cu $(NO_3)_3 \cdot 3H_2O$ was dissolved in 100 mL of Millipore water to form 0.1 M solution, B. Then, solution B was slowly added to suspension A under vigorous stirring conditions, and the pH of the mixture solution was made 12 by adding 1 M NaOH. After 15 min of stirring in a magnetic stirrer, 2 mL of 1% K_2PdCl_4 solution was added to this solution. Again, the mixture solution was magnetically stirred for another 10 min and 300 μL of NH_2-NH_2 was added as a reducing agent. The black precipitate was filtered, repeatedly washed with water and alcohol, and dried to get powdery Pd/Bi_2MoO_6-$Bi_2O_2CO_3$-CuO (Pd/BM-BOCC) nanoparticles. The Pd/ $Bi_2O_2CO_3$-Bi_2MoO_6 (Pd/BM-BOC) was synthesized with the addition of 1% K_2PdCl_4 solution as a Pd dopant and hydrazine hydrate as a reducing agent to obtain pure $Bi_2O_2CO_3$-Bi_2MoO_6 nanoparticles by the above-mentioned chemical reduction method. The Pd/CuO was also prepared with the same process mentioned above without taking $Bi_2O_2CO_3$-Bi_2MoO_6 nanoparticles.

4.5. Structural Characterization. The crystal structure and phase purity of the synthesized nanocatalysts were characterized by X-ray diffraction (XRD) with an X-ray diffractometer Bruker D8 Advance operated at 40 kV and 40 mA using a Cu Kα radiation source (λ = 1.5418Å). The relative composition of the quaternary catalyst was calculated using Rietveld analysis of PXRD data. The morphological features of the catalysts were investigated using a field emission scanning electron microscope attached with an energy dispersive X-ray spectrometer (EDS) and elemental mapping (FESEM, INSPECT F50 FEI), transmission electron microscopy (TEM), and high-resolution transmission electron microscopy (JEM-2100F HRTEM, JEOL, Japan), and selected area electron diffraction (SAED). XPS spectra of the Pd/BM-BOCC composite were obtained by using Thermo Fisher Scientific Inc., U.K. An X-ray source operated at 150W (12 kV, 12.5 mA) was used as nonmonochromatic Al Kα radiation

(1486.6 eV). The physicochemical and optical characteristics were studied using an UV–visible spectrophotometer (V-630, Jasco, Japan) and photoluminescence spectra (RF-5301, Shimadzu, Japan). Ex situ Fourier transform infrared spectroscopy (FTIR, Perkin Elmer, Spectrum RX1, Resolution 4 cm^{-1}) was applied to characterize the catalysts and for the identification of ethanol oxidation intermediate products.

4.6. Fabrication of the As-Prepared Electrodes. For fabrication of the electrodes, 2 mg of the as-prepared catalysts was suspended in 1 mL of ethanol by 30 min of sonication. 10 μL of aliquot suspension was drop-cast onto the polished and cleaned graphite carbon electrode surface and then dried for 2 h. At last, 5 μL of 1(w/v)% Nafion solution is drop-cast on the top of the electrode and dried overnight to fix the electrocatalysts.[14,50]

4.7. Photo-electrochemical Analysis. The photo-electrochemical investigation was carried out with an AUTOLAB potentiostat at room temperature using a standard three-electrode electrochemical cell. We employed the modified Pd/BM-BOC, Pd/CuO, and Pd/BM-BOCC catalysts deposited on a carbon electrode (0.12 cm^2 geometrical surface area), a large Pt foil (1 cm × 1 cm), and saturated calomel electrode (SCE) as a working electrode, counter electrode, and reference electrode, respectively. Cyclic voltammetry measurements were conducted in 1 M NaOH aqueous solution and 1 M NaOH containing 1 M EtOH solution at a potential between −0.9 V and + 0.6 V at different scan rates ranging from 1 to 300 mV s^{-1}. The chronoamperometry operation was implemented for 1000–6000 s at −0.3 V. Prior to each measurement, the solution is saturated by purging with pure nitrogen gas. CO stripping and oxidation were done in the potential range from −0.6 to +0.2 V (vs SCE electrode) using 1 M NaOH solution at a sweep rate 50 mV s^{-1}. At first, N_2 gas was purged into the solution for 20 min; after that, CO gas was bubbled for 15 min, and then, N_2 gas was again passed into the solution for 15 min to remove the excess CO adsorption. Electrochemical impedance spectroscopy (EIS) was studied at a constant potential of −0.3 V from 0.1 to 10^5 Hz frequency under 5 mV AC voltage. During all the electrochemical measurements, a 30 W LED bulb (wavelength >400 nm) was utilized as the visible light source. The light intensity was measured using a lux meter (LX-101A). The experimental framework of the photo-electrooxidation system was depicted in our earlier study.[14,16,51]

4.8. Analysis of EOR Products by FTIR and HPLC. At first, chronoamperometric measurements have been operated at a potential of −0.3 V with respect to the SCE for 7200 s in 10 mL of 1 M ethanol + 1 M NaOH solution taking Pd/Bi_2MoO_6- $Bi_2O_2CO_3$, Pd/CuO, and Pd/ Bi_2MoO_6- $Bi_2O_2CO_3$-Cu_2O nanocatalyst as working electrodes. Then, the triggered solutions were tested for FTIR and high-performance liquid chromatography (HPLC) (Shimadzu Corporation, Japan) similar to the previous study.[11,16]

■ ASSOCIATED CONTENT

ⓢ Supporting Information

The Supporting Information is available free of charge at https://pubs.acs.org/doi/10.1021/acsomega.3c02669.

> Rietveld refinement of PXRD and composition, FESEM images and EDX profiles, UV−vis spectra, Tauc plot, PL spectra, and CV and CA profiles of the synthesized catalysts, comparison table of the Pd-based material for

photo-electrooxidation of alcohol, and FESEM images of the used catalyst after the stability test (PDF)

■ AUTHOR INFORMATION

Corresponding Author

Swapan Kumar Bhattacharya − *Physical Chemistry Section, Department of Chemistry, Jadavpur University, Kolkata 700032, India;* ● orcid.org/0000-0003-4904-0954; Phone: 919831699643; Email: skbhatt7@yahoo.co.in; Fax: +913324146584

Authors

Kamal Kanti Bera − *Physical Chemistry Section, Department of Chemistry, Jadavpur University, Kolkata 700032, India*

Anupam Chowdhury − *Physical Chemistry Section, Department of Chemistry, Jadavpur University, Kolkata 700032, India*

Shyamal Kanti Bera − *School of Chemical Science, National Institute of Science Education and Research (NISER), Bhubaneswar 752050, India*

Mahima Ranjan Das − *Department of Physics, The University of Burdwan, Burdwan 713104, India*

Atanu Roy − *Department of Instrumentation Science, Jadavpur University, Kolkata 700032, India*

Sachindranath Das − *Department of Instrumentation Science, Jadavpur University, Kolkata 700032, India;* ● orcid.org/0000-0002-6938-6701

Complete contact information is available at:
https://pubs.acs.org/10.1021/acsomega.3c02669

Author Contributions

K.K.B.: conceptualization, methodology, investigation, visualization, data analysis, and writing—original draft; S.K.B.: FESEM, EDAX, elemental mapping, TEM, and HRTEM measurements; A.C., A.R., M.R.D.: investigation and software; S.D.: formal analysis; and S.K.B.: supervision, methodology, formal analysis, and writing and editing.

Notes

The authors declare no competing financial interest.

■ ACKNOWLEDGMENTS

■ REFERENCES

(1) Ehsani, A.; Heidari, A.; Asgari, R. Electrocatalytic Oxidation of Ethanol on the Surface of Graphene Based Nanocomposites: An Introduction and Review to it in Recent Studies. *Chem. Rec.* 2019, 19, 2341−2360.

(2) Chowdhury, S. R.; Maiyalagan, T.; Bhattacharaya, S. K.; Gayen, A. Influence of Phosphorus on the Electrocatalytic Activity of Palladium Nickel Nanoalloy Supported on N-Doped Reduced Graphene Oxide for Ethanol Oxidation Reaction. *Electrochim. Acta* 2020, 342, No. 136028.

(3) Yaqoob, L.; Noor, T.; Iqbal, N. A Comprehensive and Critical Review of the Recent Progress in Electrocatalysts for the Ethanol Oxidation Reaction. *RSC Adv.* 2021, 11, 16768−16804.

(4) Mukherjee, P.; Roy, P. S.; Mandal, K.; Bhattacharjee, D.; Dasgupta, S.; Bhattacharya, S. K. Improved Catalysis of Room Temperature Synthesized Pd-Cu Alloy Nanoparticles for Anodic Oxidation of Ethanol in Alkaline Media. *Electrochim. Acta* 2015, 154, 447−455.

(5) Zhong, J. P.; Hou, C.; Li, L.; Waqas, M.; Fan, Y. J.; Shen, X. C.; Sun, S. G.; et al. A Novel Strategy for Synthesizing Fe, N, and S Tridoped Graphene-Supported Pt Nanodendrites toward Highly Efficient Methanol Oxidation. *J. Catal.* 2020, 381, 275−284.

(6) Xiang, S.; Wang, L.; Huang, C. C.; Fan, Y. J.; Tang, H. G.; Wei, L.; Sun, S. G. Concave Cubic Pt/La Alloy Nanocrystals with High-index Facets: Controllable Synthesis in Deep Eutectic Solvents and Their Superior Electrocatalytic Properties for Ethanol Oxidation. *J. Power Sources* 2018, 399, 422−428.

(7) Zhong, J.; Li, L.; Waqas, M.; Wang, X.; Fan, Y.; Qi, J.; Sun, S.; et al. Deep Eutectic Solvent-assisted Synthesis of Highly Efficient Pt-Cu Alloy Nanoclusters on Carbon Nanotubes for Methanol Oxidation Reaction. *Electrochim. Acta* 2019, 322, 134677−134685.

(8) Fan, J. J.; Fan, Y. J.; Wang, R. X.; Xiang, S.; Tang, H. G.; Sun, S. G. A Novel Strategy for the Synthesis of Sulfur-Doped Carbon Nanotubes as a Highly Efficient Pt Catalyst Support toward the Methanol Oxidation Reaction. *J. Mater. Chem. A* 2017, 5, 19467−19475.

(9) Bai, J.; Liu, D.; Yang, J.; Chen, Y. Nanocatalysts for Electrocatalytic Oxidation of Ethanol. *Chem. Sus. Chem.* 2019, 12, 2117−2132.

(10) Roy Chowdhury, S.; Banik, M. S.; Mahajan, A.; Bhattacharya, S. K. Anode Catalytic Activity of Palladium-Nickel Alloy Nanoparticles for Ethanol Oxidation in Alkali. *ChemistrySelect* 2020, 5, 9848−9856.

(11) Chowdhury, S. R.; Bera, K. K.; Ray, A.; Bera, P. S.; Maiyalagan, T.; Bhattacharya, S. K. Synergistic catalytic activity of palladium—silver alloy nanoparticle for anodic oxidation of ethanol in alkali. *Int. J. Hydrogen Energy* 2021, 46, 14212−14224.

(12) Yang, Y. Y.; Ren, J.; Li, Q. X.; Zhou, Z. Y.; Sun, S. G.; Cai, W. B. Electrocatalysis of Ethanol on a Pd electrode in Alkaline Media: an in Situ Attenuated Total Reflection Surface-Enhanced Infrared Absorption Spectroscopy Study. *ACS Catal.* 2014, 4, 798−803.

(13) Hao, J. F.; Liu, B.; Takahashi, M.; Maenosono, S.; Yang, J. Large Au@ Pd/PdOx Core-Porous Shell Nanoparticles as Efficient Ethanol Oxidation Electrocatalysts. *Catal. Sci. Technol.* 2023, 13, 4141−4147.

(14) Chakraborty, M.; Bera, K. K.; Mandal, M.; Ghorai, K.; Sepay, N. Visible Light Assisted Photo-Electrocatalytic Oxidation of Methanol using Low Pt Content NiO-rutile TiO_2 Ternary Heterojunction. *Appl. Surf. Sci.* 2020, 541, 148450−148464.

(15) Fuku, X.; Modibedi, M.; Matinise, N.; Mokoena, P.; Xaba, N.; Mathe, M. Single Step Synthesis of Bio-inspired NiO/C as Pd Support Catalyst for Dual Application: Alkaline Direct Ethanol Fuel Cell and CO_2 Electro-Reduction. *J. Colloid Interface Sci.* 2019, 545, 138−152.

(16) Bera, K. K.; Chakraborty, M.; Bera, S. K.; Chowdhury, A.; Das, M. R.; Mondal, M.; Bhattacharya, S. K. Synergistic Photo-Enhanced Electrocatalysis of Pt−ZnO−Bi_2O_3 Heterojunction for Methanol Oxidation under Visible Light Illumination. *Energy Adv.* 2022, 1, 908−925.

(17) Rostami, H.; Rostami, A. A.; Omrani, A. An Electrochemical Method to Prepare of Pd/Cu_2O/MWCNT Nanostructure as an Anode Electrocatalyst for Alkaline Direct Ethanol Fuel Cells. *Electrochim. Acta* 2016, 194, 431−440.

(18) Ipadeola, A. K.; Barik, R.; Ray, S. C.; Ozoemena, K. I. Bimetallic Pd/SnO_2 Nanoparticles on Metal Organic Framework (MOF)-Derived Carbon as Electrocatalysts for Ethanol Oxidation. *Electrocatalysis* 2019, 10, 366−380.

(19) Gao, F.; Zhang, Y.; Wu, Z.; You, H.; Du, Y. Universal Strategies to Multi-dimensional Noble-Metal-Based Catalysts for Electrocatalysis. *Coord. Chem. Rev.* 2021, 436, 213825−213848.

(20) Gao, F.; Zhang, Y.; Ren, F.; Shiraishi, Y.; Du, Y. Universal Surfactant-Free Strategy for Self-Standing 3D Tremella-like Pd−M (M= Ag, Pb, and Au) Nanosheets for Superior Alcohols Electrocatalysis. *Adv. Funct. Mater.* 2020, 30, 2000255−2000264.

(21) El Attar, A.; Oularbi, L.; Chemchoub, S.; El Rhazi, M. Effect of Electrochemical Activation on the Performance and Stability of Hybrid (PPy/Cu2O Nanodendrites) for Efficient Ethanol Oxidation in Alkaline Medium. *J. Electroanal. Chem.* 2021, 885, No. 115042.

(22) Zhang, J.; Liu, Z.; Ma, Z. Facile Formation of $Bi_2O_2CO_3$/Bi_2MoO_6 Nanosheets for Visible Light-Driven Photocatalysis. *ACS Omega* 2019, 4, 3871−3880.

(23) Safaei, J.; Ullah, H.; Mohamed, N. A.; Noh, M. F. M.; Soh, M. F.; Tahir, A. A.; Teridi, M. A. M.; et al. Enhanced Photoelectrochemical Performance of Z-scheme $g-C_3N_4$/$BiVO_4$ Photocatalyst. *Appl. Catal., B* 2018, 234, 296−310.

(24) Li, L.; Gao, H.; Liu, G.; Wang, S.; Yi, Z.; Wu, X.; Yang, H. Synthesis of Carnation Flower-Like $Bi_2O_2CO_3$ Photocatalyst and its Promising Application for Photoreduction of Cr (VI). *Adv. Powder Technol.* 2022, 33, No. 103481.

(25) Yang, Z.; Shen, M.; Dai, K.; Zhang, X.; Chen, H. Controllable Synthesis of Bi_2MoO_6 Nanosheets and their Facet-Dependent Visible-Light-Driven Photocatalytic Activity. *Appl. Surf. Sci.* 2018, 430, 505−514.

(26) Zhang, X.; Ren, G.; Zhang, C.; Xue, J.; Zhao, Q.; Li, R.; Wang, Y.; Fan, C. Assisting Bi_2MoO_6 Microspheres with Phenolic Resin-Based ACSs as Attractive Tailor-Made Supporter for Highly-Efficient Photocatalytic CO_2 Reduction. *Green Energy Environ.* 2021, 6, 693−702.

(27) Ma, T.; Jin, S.; Kong, X.; Lv, M.; Wang, H.; Luo, X.; Song, X.; et al. Plasma Engraved Bi_2MoO_6 Nanosheet Arrays towards High Performance Supercapacitor and Oxygen Evolution Reaction. *Appl. Surf. Sci.* 2021, 548, 149244−149253.

(28) Zhang, Y.; Gao, F.; Wang, D.; Li, Z.; Wang, X.; Wang, C.; Zhang, K.; Du, Y. Amorphous/Crystalline Heterostructure Transition-Metal-Based Catalysts for High-Performance Water Splitting. *Coord. Chem. Rev.* 2023, 475, 214916−214934.

(29) Zhang, Y.; Wang, D.; Ye, C.; Gao, F.; Li, Z.; Du, Y. Regulation of Crystallinity and Defects on CoNiRuOx Nanocages for Enhanced Oxygen Evolution Reaction. *Chem. Eng. J.* 2023, 466, 143059−143068.

(30) Li, J. H.; Ren, J.; Hao, Y. J.; Zhou, E. P.; Wang, Y.; Wang, X. J.; Li, F. T.; et al. Construction of β-Bi_2O_3/$Bi_2O_2CO_3$ Heterojunction Photocatalyst for Deep Understanding the Importance of Separation Efficiency and Valence Band Position. *J. Hazard. Mater.* 2021, 401, 123262−123273.

(31) Meng, X.; Li, Z.; Yun, N.; Zhang, Z. A Comparison of Pd^0 Nanoparticles and Pd^{2+} Modified $Bi_2O_2CO_3$ for Visible Light-Driven Photocatalysis. *J. Nanomater.* 2018, 2018, No. 1234506.

(32) Lin, S.; Cui, W.; Li, X.; Sui, H.; Zhang, Z. Cu_2O NPs/$Bi_2O_2CO_3$ Flower-Like Complex Photocatalysts with Enhanced Visible Light Photocatalytic Degradation of Organic Pollutants. *Catal. Today,* 2017, 297, 237−245.

(33) Huang, Y.; Fan, W.; Long, B.; Li, H.; Zhao, F.; Liu, Z.; Tong, Y.; Ji, H. Visible Light Bi_2S_3/Bi_2O_3/$Bi_2O_2CO_3$ Photocatalyst for Effective Degradation of Organic Pollutions. *Appl. Catal., B* 2016, 185, 68−76.

(34) Xu, Y. S.; Zhang, W. D. Anion Exchange Strategy for Construction of Sesame-Biscuit-Like $Bi_2O_2CO_3$/Bi_2MoO_6 Nanocomposites with Enhanced Photocatalytic Activity. *Appl. Catal., B* 2013, 140−141, 306−316.

(35) Wang, J.; Jia, X.; Shang, D.; Xie, L.; Li, Y.; Zhang, H.; Zhan, S.; Hu, W. Constructing Cu_2O/Bi_2MoO_6 p−n Heterojunction towards Boosted Photo-Assisted-Electro-Fenton-Like Synergy Degradation of Ciprofloxacin. *Environ. Sci. Nano.* 2021, 8, 3629−3642.

(36) Xu, X.; Meng, L.; Dai, Y.; Zhang, M.; Sun, C.; Yang, S.; Li, H.; et al. Bi Spheres SPR-Coupled Cu_2O/Bi_2MoO_6 with Hollow Spheres Forming Z-scheme Cu_2O/Bi/Bi_2MoO_6 Heterostructure for Simultaneous Photocatalytic Decontamination of Sulfadiazine and Ni (II). *J. Hazard. Mater.* 2020, 381, 120953−120966.

(37) Lin, X.; Guo, X.; Shi, W.; Zhai, H.; Yan, Y.; Wang, Q. Quaternary Heterostructured $Ag−Bi_2O_2CO_3$/$Bi_{3.64}$ $Mo_{0.36}O_{6.55}$/Bi_2MoO_6 Composite: Synthesis and Enhanced Visible-Light-Driven Photocatalytic Activity. *J. Solid State Chem.* 2015, 229, 68−77.

(38) Zou, J. P.; Luo, S. L.; Zhang, L. Z.; Ma, J.; Lei, S. L.; Zhang, L. S.; Au, C. T.; et al. One-Pot Solvothermal Syntheses of Ternary Heterostructured $TiO_2−Bi_2MoO_6$/$Bi_{3.64}Mo_{0.36}O_{6.55}$ Controllable in Terms of Composition, Morphology and Structure: Materials of High Visible-Light Driven Photocatalytic Activity. *Appl. Catal., B* 2013, 140−141, 608−618.

(39) Xiang, S.; Zhang, Z.; Wu, Z.; Sun, L.; Radjenovic, P.; Ren, H.; Li, J.; et al. 3D Heterostructured Ti-based Bi_2MoO_6/Pd/TiO_2 Photocatalysts for High-Efficiency Solar Light Driven Photoelectrocatalytic Hydrogen Generation. *ACS Appl. Energy Mater.* 2019, 2, 558−568.

(40) Shu, Y.; Zheng, Y.; Ying, Y.; Yu, G.; Wu, Y.; Wen, Y.; Yang, H. Metal and Metal Oxide Interaction in Hollow CuO/Pd Catalyst Boosting Ethanol Electrooxidation. *J. Electrochem. Soc.* 2020, 167, 064508−064517.

(41) Anantharaj, S.; Sugime, H.; Noda, S. Ultrafast Growth of a $Cu(OH)_2−CuO$ Nanoneedle Array on Cu Foil for Methanol Oxidation Electrocatalysis. *ACS Appl. Mater. Interfaces* 2020, 12, 27327−27338.

(42) Ali, S.; Razzaq, A.; Kim, H.; In, S. I. Activity, Selectivity, and Stability of Earth-Abundant CuO/Cu_2O/Cu(0)-Based Photocatalysts Toward CO_2 Reduction. *Chem. Eng. J.* 2022, 429, 131579−131648.

(43) Wang, H.; Wang, Y.; Jiang, C.; Ye, K.; He, X.; Xue, C.; Ji, H.; et al. Hybridization of CuO with Bi_2MoO_6 Nanosheets as a Surface Multifunctional Photocatalyst for Toluene Oxidation Under Solar Irradiation. *ACS Appl. Mater. Interfaces* 2020, 12, 2259−2268.

(44) El Attar, A.; Chemchoub, S.; Kalan, M. D.; Oularbi, L.; El Rhazi, M. Designing New Material Based on Functionalized Multi-Walled Carbon Nanotubes and $Cu(OH)_2−Cu_2O$/Polypyrrole Catalyst for Ethanol Oxidation in Alkaline Medium. *Front. Chem.* 2021, 9, No. 805654.

(45) Yang, Q.; Qin, Y.; Chu, S.; Sun, S.; Liu, D.; Yang, S.; Liang, S. Preparation of Nanoporous Cu/Cu_2O Composites by Anodic Oxidation and Their Electrocatalytic Performance Towards Methanol Oxidation. *Mater. Today Commun.* 2021, 26, No. 101992.

(46) Song, T.; Gao, F.; Jin, L.; Zhang, Y.; Wang, C.; Li, S.; Chen, C.; Du, Y. From Bimetallic PdCu Nanowires to Ternary PdCu-SnO_2 Nanowires: Interface Control for Efficient Ethanol Electrooxidation. *J. Colloid Interface Sci.* 2020, 560, 802−810.

(47) Alvarenga, G. M.; Gallo, I. B. C.; Villullas, H. M. Enhancement of Ethanol Oxidation on Pd Nanoparticles Supported on Carbon-Antimony Tin Oxide Hybrids Unveils the Relevance of Electronic effects. *J. Catal.* 2017, 348, 1−8.

(48) Halim, E. M.; Perrot, H.; Sel, O.; Debiemme-Chouvy, C.; Lafdi, K.; El Rhazi, M. Electrosynthesis of Hierarchical $Cu_2O−Cu(OH)_2$ Nanodendrites Supported on Carbon Nanofibers/Poly(Para-Phenylenediamine) Nanocomposite as High-Efficiency Catalysts for Methanol Electrooxidation. *Int. J. Hydrogen Energy* 2021, 46, 19926−19938.

(49) Ji, Y.; Ying, Y.; Pan, Y.; Li, M.; Guo, X.; Wu, Y.; Wen, Y.; Yang, H. Palladium Networks Decorated by Cuprous Oxide for Remarkably Enhanced Electrocatalytic Activity of Methanol Oxidation Reaction with High CO-Tolerance. *J. Power Sources* 2016, 329, 115−122.

(50) Bera, K. K.; Chakraborty, M.; Chowdhury, S. R.; Ray, A.; Das, S.; Bhattacharya, S. K. Significantly Improved and Synergistic Effect of $Pt−ZnO−Bi_2O_3$ Ternary Heterojunctions Toward Anode-Catalytic Oxidation of Methanol in Alkali. *Electrochim. Acta* 2019, 322, No. 134775.

(51) Bera, K. K.; Chakraborty, M.; Bera, S. K.; Roy, P. S.; Mandal, M.; Chatterjee, S.; Bhattacharya, S. K. Synthesis of Different Pt-ZnO Binary Junctions for Photo Electrocatalytic Oxidation of Methanol in Alkali. *ChemistrySelect* 2021, 6, 6586−6596.

(52) Meng, X.; Zhang, Z. Bi_2MoO_6 Co-modified by Reduced Graphene Oxide and Palladium (Pd^{2+} and Pd^0) with Enhanced

Photocatalytic Decomposition of Phenol. *Appl. Catal., B* **2017**, *209*, 383−393.

(53) Wang, M.; Zhang, Y.; Jin, C.; Li, Z.; Chai, T.; Zhu, T. Fabrication of Novel Ternary Heterojunctions of Pd/g-C_3N_4/Bi_2MoO_6 Hollow Microspheres for enhanced Visible-Light Photocatalytic Performance Toward Organic Pollutant Degradation. *Sep. Purif. Technol.* **2019**, *211*, 1−9.

(54) Salari, H. Facile Synthesis of New Z-Scheme Bi_2WO_6/Bi_2MoO_6 p−n Junction Photocatalysts with High Photocatalytic Activity: Structure, Kinetics and Mechanism Approach. *Mater. Res. Bull.* **2020**, *131*, No. 110979.

(55) Kandi, D.; Martha, S.; Thirumurugan, A.; Parida, K. M. CdS QDs-Decorated Self-Doped γ-Bi_2MoO_6: A Sustainable and Versatile Photocatalyst Toward Photoreduction of Cr (VI) and Degradation of Phenol. *ACS Omega* **2017**, *2*, 9040−9056.

(56) Li, H.; Luo, X.; Long, Z.; Huang, G.; Zhu, L. Plasmonic Ag Nanoparticle-Loaded n-p $Bi_2O_2CO_3$/α-Bi_2O_3 Heterojunction Microtubes with Enhanced Visible-Light-Driven Photocatalytic Activity. *J. Nanomater.* **2022**, *12*, 1608.

(57) Bhat, A. A.; Thoker, B. A.; Wani, A. K.; Sheergojri, G. A.; Kaloo, M. A.; Bhatd, B. A.; Rizvie, S. M. A. Synthesis and Characterization of Copper Oxide Nanoparticles by Coprecipitation Method: Electronic and Antimicrobial Properties. *Chem. Sci. Eng. Res.* **2021**, *3*, 25−29.

(58) Li, H.; Luo, X.; Long, Z.; Huang, G.; Zhu, L. Plasmonic Ag Nanoparticle-Loaded n-p $Bi_2O_2CO_3$/α-Bi_2O_3 Heterojunction Microtubes with Enhanced Visible-Light-Driven Photocatalytic Activity. *Nanomaterials* **2022**, *12*, 1608−1623.

(59) Ortiz-Quiñonez, J. L.; Vega-Verduga, C.; Díaz, D.; Zumeta-Dube, I. Transformation of Bismuth and β-Bi_2O_3 Nanoparticles into $(BiO)_2CO_3$ and $(BiO)_4(OH)_2CO_3$ by Capturing CO_2: the Role of Halloysite Nanotubes and "Sunlight" On the Crystal Shape and Size. *Cryst. Growth Des.* **2018**, *18*, 4334−4346.

(60) Chen, Q.; Lan, X.; Zhu, G.; Wang, L.; Shi, J. Facile One-step Redox Synthesis of $Bi_2O_2CO_3$/Bi_2O_3/Bi Ternary Photocatalyst without Additional Carbon Source. *J. Mater. Sci.: Mater. Electron.* **2021**, *32*, 15466−15474.

(61) Leclerc, M.; Etxebarria, A.; Ye, Y.; Crumlin, E. J.; Brisard, G. M. An APXPS Probe of Cu/Pd Bimetallic Catalysts Surface Chemistry of CO_2 Toward CO in the Presence of H_2O and H_2. *J. Phys. Chem. C* **2020**, *124*, 17085−17094.

(62) Shinde, P. V.; Shinde, N. M.; Yun, J. M.; Mane, R. S.; Kim, K. H. Facile Chemical Synthesis and Potential Supercapattery Energy Storage Application of Hydrangea-Type Bi_2MoO_6. *ACS Omega* **2019**, *4*, 11093−11102.

(63) Li, Z.; Zhang, T. C.; Mokoba, T.; Yuan, S. Superwetting Bi_2MoO_6/$Cu_3(PO4)_2$ Nanosheet-Coated Copper Mesh with Superior Anti-Oil-Fouling and Photo-Fenton-Like Catalytic Properties for Effective Oil-in-Water Emulsion Separation. *ACS Appl. Mater. Interfaces* **2021**, *13*, 23662−23674.

(64) Bai, P.; Tong, X.; Wan, J.; Gao, Y.; Xue, S. Flower-Like $Bi_2O_2CO_3$-Mediated Selective Oxidative Coupling Processes of Amines Under Visible Light Irradiation. *J. Catal.* **2019**, *374*, 257−265.

(65) Maswanganyi, S.; Gusain, R.; Kumar, N.; Fosso-Kankeu, E.; Waanders, F. B.; Ray, S. S. Bismuth Molybdate nanoplates supported on Reduced Graphene Oxide: An Effective Nanocomposite for the Removal of Naphthalene via Adsorption−Photodegradation. *ACS Omega* **2021**, *6*, 16783−16794.

(66) Zhou, J.; Pan, J.; Jin, Y.; Peng, Z.; Xu, Z.; Chen, Q.; Wu, K.; et al. Single-Cation Catalyst: Ni Cation in Monolayered CuO for CO Oxidation. *J. Am. Chem. Soc.* **2022**, *144*, 8430−8433.

(67) Wang, H.; Guo, Y.; Li, C.; Yu, H.; Deng, K.; Wang, Z.; Wang, L.; et al. Cu/CuO_x In-Plane Heterostructured Nanosheet Arrays with Rich Oxygen Vacancies Enhance Nitrate Electroreduction to Ammonia. *ACS Appl. Mater. Interfaces* **2022**, *14*, 34761−34769.

(68) Wang, A.; Guan, J.; Zhang, L.; Wang, H.; Ma, G.; Fan, G.; Chen, Y.; et al. In Situ Synthesis of Monolithic Cu_2O−CuO/Cu Catalysts for Effective Ozone Decomposition. *J. Phys. Chem. C* **2022**, *126*, 317−325.

(69) Zhang, Y.; Gao, F.; You, H.; Li, Z.; Zou, B.; Du, Y. Recent Advances in One-dimensional Noble-Metal-Based Catalysts with Multiple Structures for Efficient Fuel-Cell Electrocatalysis. *Coord. Chem. Rev.* **2022**, *450*, 214244−214263.

(70) Wang, Z.; Lin, R.; Huo, Y.; Li, H.; Wang, L. Formation, Detection, and Function of Oxygen Vacancy in Metal Oxides for Solar Energy Conversion. *Adv. Funct. Mater.* **2022**, *32*, 2109503−2109518.

(71) Cheng, W.; Guan, W.; Lin, Y.; Lu, C. Rapid Discrimination of Adsorbed Oxygen and Lattice Oxygen in Catalysts by the Cataluminescence Method. *Anal. Chem.* **2022**, *94*, 1382−1389.

(72) Fu, Y.; Zhang, Y.; Wei, L.; Du, H.; Yan, Q. Er^{3+}/Sm^{3+} Co-doped $Bi_2O_2CO_3$ in Photocatalytic Water Treatment: Immobilization, Acute Toxicity, Sterilization, and Catalytic Oxidation Activity. *Chemosphere* **2022**, *306*, No. 135507.

(73) Su, D.; Xie, X.; Dou, S.; Wang, G. CuO Single Crystal with Exposed {001} Facets-A Highly Efficient Material for Gas Sensing and Li-ion Battery Applications. *Sci. Rep.* **2014**, *4*, No. 5753.

(74) Bera, K. K.; Majumdar, R.; Chakraborty, M.; Bhattacharya, S. K. Phase Control Synthesis of α, β and α/β Bi_2O_3 Hetero-junction with Enhanced and Synergistic Photocatalytic Activity on Degradation of toxic dye, Rhodamine-B under natural sunlight. *J. Hazard. Mater* **2018**, *352*, 182−191.

(75) Bera, K. K.; Chakraborty, M.; Mondal, M.; Banik, S.; Bhattacharya, S. K. Synthesis of α-β Bi_2O_3 heterojunction photocatalyst and Evaluation of Reaction Mechanism for Degradation of RhB Dye Under Natural Sunlight. *Ceram. Int.* **2020**, *46*, 7667−7680.

(76) Nayak, R.; Ali, F. A.; Mishra, D. K.; Ray, D.; Aswal, V. K.; Sahoo, S. K.; Nanda, B. Fabrication of CuO Nanoparticle: An Efficient Catalyst Utilized for Sensing and Degradation of Phenol. *J. Mater. Res. Technol.* **2020**, *9*, 11045−11059.

(77) Sharma, P.; Minakshi Sundaram, M.; Singh, D.; Ahuja, R. Highly Energetic and Stable Gadolinium/Bismuth Molybdate with a Fast Reactive Species, Redox Mechanism of Aqueous Electrolyte. *ACS Appl. Energy Mater.* **2020**, *3*, 12385−12399.

(78) Luo, Y.; Zheng, A.; Li, J.; Han, Y.; Xue, M.; Zhang, L.; Xie, X.; et al. Integrated Adsorption and Photodegradation of Tetracycline by Bismuth Oxycarbonate/Biochar Nanocomposites. *Chem. Eng. J.* **2023**, *457*, No. 141228.

(79) Collu, D. A.; Carucci, C.; Piludu, M.; Parsons, D. F.; Salis, A. Aurivillius Oxides Nanosheets-Based Photocatalysts for Efficient Oxidation of Malachite Green Dye. *Int. J. Mol. Sci.* **2022**, *23*, 5422−5440.

(80) Yu, Z.; Moussa, H.; Liu, M.; Schneider, R.; Moliere, M.; Liao, H. Heterostructured Metal Oxides-ZnO Nanorods Films Prepared by SPPS Route for Photodegradation Applications. *Surf. Coat. Technol.* **2019**, *375*, 670−680.

(81) White, J.; Anil, A.; Martín-Yerga, D.; Salazar-Alvarez, G.; Henriksson, G.; Cornell, A. Electrodeposited PdNi on a Ni Rotating Disk Electrode Highly Active for Glycerol Electrooxidation in Alkaline Conditions. *Electrochim. Acta* **2022**, *403*, No. 139714.

(82) Zhou, D.; Du, R.; Hu, Z.; Gao, S.; Tu, Y.; Fu, Y.; Zheng, G.; Zhou, Y. Fabrication of Bi_2MoO_6 Nanosheets/TiO_2 Nanorod Arrays Heterostructures for Enhanced Photocatalytic Performance under Visible-Light Irradiation. *Nanomaterials* **2022**, *12*, 574−588.

(83) Zhu, M.; Zhai, C.; Sun, M.; Hu, Y.; Yan, B.; Du, Y. Ultrathin Graphitic C_3N_4 Nanosheet as a Promising Visible-Light-Activated Support for Boosting Photoelectrocatalytic Methanol Oxidation. *Appl. Catal., B* **2017**, *203*, 108−115.

(84) Sun, M.; Hu, J.; Zhai, C.; Zhu, M.; Pan, J. (2017). A p-n Heterojunction of CuI/TiO_2 with Enhanced Photoelectrocatalytic Activity for Methanol Electro-Oxidation. *Electrochim. Acta* **2017**, *245*, 863−871.

(85) Sharma, M.; Das, B.; Hazarika, A.; Guha, A. K.; Bhargava, S. K.; Bania, K. K. PdO/CuO Nanoparticles on Zeolite-Y for Nitroarene Reduction and Methanol Oxidation. *ACS Appl. Nano Mater.* **2019**, *2*, 3769−3779.

(86) Chen, Z.; Liu, Y.; Liu, C.; Zhang, J.; Chen, Y.; Hu, W.; Deng, Y. Engineering the Metal/Oxide Interface of Pd Nanowire@CuO_x

Electrocatalysts for Efficient Alcohol Oxidation Reaction. *Small* **2020**, *16*, No. 1904964.

(87) Zhang, S.; Pei, A.; Li, G.; Zhu, L.; Li, G.; Wu, F.; Luque, R.; et al. Pd/CuO−Ni(OH)$_2$/C as a Highly Efficient and Stable Catalyst for the Electrocatalytic Oxidation of Ethanol. *Green Chem.* **2022**, *24*, 2438−2450.

(88) Krittayavathananon, A.; Duangdangchote, S.; Pannopard, P.; Chanlek, N.; Sathyamoorthi, S.; Limtrakul, J.; Sawangphruk, M. Elucidating the Unexpected Electrocatalytic Activity of Nanoscale PdO Layers on Pd Electrocatalysts towards Ethanol Oxidation in a Basic Solution. *Sustainable Energy Fuels* **2020**, *4*, 1118−1125.

(89) Almeida, C. V.; Eguiluz, K. I.; Salazar-Banda, G. R. Superior Ethanol Electrooxidation Activity of Pd Supported on Ni (OH)$_2$/C. The Effect of Ni(OH)$_2$ Nanosheets Content. *J. Electroanal. Chem.* **2020**, *878*, 114683−114693.

(90) Wang, S.; Lu, A.; Zhong, C. J. Hydrogen Production from Water Electrolysis: Role of Catalysts. *Nano Convergence* **2021**, *8*, No. 4.

(91) Roy, S.; Payra, S.; Challagulla, S.; Arora, R.; Roy, S.; Chakraborty, C. Enhanced Photoinduced Electrocatalytic Oxidation of Methanol using Pt Nanoparticle-Decorated TiO$_2$−Polyaniline Ternary Nanofibers. *ACS Omega* **2018**, *3*, 17778−17788.

(92) El Attar, A.; Oularbi, L.; Chemchoub, S.; El Rhazi, M. Preparation and Characterization of Copper Oxide Particles/ Polypyrrole (Cu$_2$O/PPy) via Electrochemical Method: Application in Direct Ethanol Fuel Cell. *Int. J. Hydrogen Energy* **2020**, *45*, 8887−8898.

(93) Wang, Y.; Zou, S.; Cai, W. B. Recent Advances on Electro-Oxidation of Ethanol on Pt- and Pd-Based Catalysts: From Reaction Mechanisms to Catalytic Materials. *Catalysts* **2015**, *5*, 1507−1534.

(94) Niu, M.; Xu, W.; Zhu, S.; Liang, Y.; Cui, Z.; Yang, X.; Inoue, A. Synthesis of Nanoporous CuO/TiO$_2$/Pd-NiO Composite Catalysts by Chemical Dealloying and their Performance for Methanol and Ethanol Electro-oxidation. *J. Power Sources* **2017**, *362*, 10−19.

(95) Sun, K.; Zhou, H.; Li, X.; Ma, X.; Zhang, D.; Li, M. The Novel 2-Dimensional Bi$_2$MoO$_6$-Bi$_2$O$_3$-Ag$_3$PO$_4$ Ternary Photocatalyst with n-n-p Heterojunction for Enhanced Degradation Performance. *J. Alloys Compd.* **2022**, *913*, No. 165119.

(96) Bian, Y.; Ma, Y.; Shang, Y.; Tan, P.; Pan, J. Self-Integrated β-Bi$_2$O$_3$/Bi$_2$O$_{2.33}$@ Bi$_2$O$_2$CO$_3$ Ternary Composites: Formation Mechanism and Visible Light Photocatalytic Activity. *Appl. Surf. Sci.* **2018**, *430*, 613−624.

(97) Subha, N.; Mahalakshmi, M.; Myilsamy, M.; Neppolian, B.; Murugesan, V. The Influence of n-type and p-type Dopants on the Interfacial Charge Transfer and the Band Structure of Bi$_2$MoO$_6$ to Enhance Solar H$_2$ Production. *J. Photochem. Photobiol A: Chem.* **2019**, *379*, 150−158.